REVIEW ARTICLE

Laser Rayleigh scattering

Richard B Miles[1], Walter R Lempert[1,2] and Joseph N Forkey[1,3]

[1] Princeton University, Department of Mechanical and Aerospace Engineering, Princeton, NJ 08544, USA

[2] The Ohio State University, Departments of Mechanical Engineering and Chemistry, Columbus, OH 43210, USA

[3] University of Pennsylvania, Pennsylvania Muscle Institute, The School of Medicine, D700 Richards Building, 3700 Hamilton Walk, Philadelphia, PA 19104-6083, USA

E-mail: miles@princeton.edu, lempert.1@osu.edu and forkey@mail.med.upenn.edu

Abstract

Rayleigh scattering is a powerful diagnostic tool for the study of gases and is particularly useful for aiding in the understanding of complex flow fields and combustion phenomena. Although the mechanism associated with the scattering, induced electric dipole radiation, is conceptually straightforward, the features of the scattering are complex because of the anisotropy of molecules, collective scattering from many molecules and inelastic scattering associated with rotational and vibrational transitions. These effects cause the scattered signal to be depolarized and to have spectral features that reflect the pressure, temperature and internal energy states of the gas. The very small scattering cross section makes molecular Rayleigh scattering particularly susceptible to background interference. Scattering from very small particles also falls into the Rayleigh range and may dominate the scattering from molecules if the particle density is high. This particle scattering can be used to enhance flow visualization and velocity measurements, or it may be removed by spectral filtering. New approaches to spectral filtering are now being applied to both Rayleigh molecular scattering and Rayleigh particle scattering to extract quantitative information about complex gas flow fields. This paper outlines the classical properties of Rayleigh scattering and reviews some of the new advances in flow field imaging that have been achieved using the new filter approaches.

1. Introduction

Laser-illuminated Rayleigh scattering is rapidly becoming an important diagnostic tool, whose development is being pushed by two primary drivers. The first is the use of the intensity of the Rayleigh scattering to determine flow field and flame structure as well as density and, in some cases, mixture fraction (Dyer 1979, Escoda and Long 1983). If the pressure is known, then the density measurement can be converted to temperature by assuming a known ideal gas mixture (Dibble and Hollenbach 1981). The second driver is the use of the spectrum of the Rayleigh scattering for understanding the properties of the atmosphere (Shimizu *et al* 1983) and properties of complex flows (Miles and Lempert 1997). In most cases this involves Rayleigh scattering from air or air containing a fog of particles (Samimy and Wernet 2000), and leads to the measurement of velocity fields. For molecular scattering, spectrally resolved Rayleigh scattering can lead to temperature and density fields as well (Seasholtz 1997, Forkey *et al* 1998). The use of Rayleigh scattering in this manner

requires a detailed understanding of the Rayleigh scattering process, including thermal and acoustic line broadening.

These applications are very different from those originally addressed by Lord Rayleigh, Jean Cabannes and others in the late 19th century (Abhyankar 1996). They were seeking to understand the origin of the intensity, colour and polarization of the atmosphere. In that case, the source was the sun, which is broadband and unpolarized, and the full spectrum of the scattered light was observed. The scattering from the sky is from a large volume rather than from a line or a plane defined by an illuminating laser. For laser Rayleigh scattering, multiple scattering and volume integration are not important issues.

Rayleigh scattering has a simple classical origin: the electrons in the atoms, molecules or small particles radiate like dipole antennas when they are forced to oscillate by an applied electromagnetic field. If the scattering sources are stationary, then this secondary radiation is phase locked to the driving electromagnetic field. In this case, each scatterer is driven by a field which is the coherent sum of the applied field and the fields from all the other scatterers. If the density of sources is high enough that they may be treated as a continuum, and if they are uniformly distributed, then the radiation cancels in all but the forward direction, where it adds coherently, leading to a change in the index of refraction of the propagating wave as shown by Ewald and Oseen (Born and Wolf 1980). In a gas, the motion of the molecules leads to microscopic density fluctuations that randomize the phases and cause the scattering to be incoherent in all but the forward direction. Away from the forward direction, very rapidly changing interferences occur which average to remove coherent effects and make the scattering intensity just proportional to the number of scatterers. In the forward direction, coherence is maintained since there is no momentum transfer. The phases add together, independent of the motion, and the Ewald–Oseen solution remains valid (Long 1977). For this reason, Rayleigh scattering is called 'coherent'. This coherent nature of the interaction means that Rayleigh scattering is sensitive to long range coherent density fluctuations associated with acoustic waves and turbulent phenomena.

The simple dipole model gives excellent results for monatomic gases such as helium and argon, where no internal degrees of freedom are present. In the case of molecules both vibrational and rotational energy states are present and add complexity to the scattering spectrum. Inelastic vibrational and rotational Raman scattering frequencies arise associated with changes of vibrational and rotational energy states during the scattering process, and the 'elastic' or Rayleigh scattering is depolarized and partially dephased, even in the forward scattering direction. Since few applications of Rayleigh scattering involve monatomic gases, these effects must be taken into account for proper analysis.

Figure 1 shows the various components of molecular light scattering at sequentially higher resolution. Molecular nitrogen at 1 atm, 300 K, is used as an example. Farthest removed from the laser wavelength are the vibrational Raman bands. These are of the order of a few hundred to a few thousand wavenumbers (cm^{-1}) away (2331 cm^{-1} for N_2). (Note: 1 cm^{-1} = 30 GHz.) Closer to the laser lines is the rotational Raman band. This consists of a series of lines associated with $\Delta J = \pm 2$ rotational transitions, the first of

which are ± 6 B coefficients displaced from the laser line. Sequential lines are spaced at 4 B intervals. B coefficients for molecules are inversely proportional to the molecular weight and are of the order of a few cm^{-1} (1.99 cm^{-1} for N_2).

The central feature is associated with elastic scattering and does not change the internal energy of the molecule. It lies closest to the laser line and has features that reflect the translational motion. If the motion is collision dominated (hydrodynamic limit), acoustic sidebands are present at frequency shifts associated with the speed of sound in the medium and the line shapes are Lorentzian. At low pressure or high temperature, the molecular motion is thermally dominated and the scattering lineshape takes the form of a thermally broadened Gaussian profile. For 1 atm of nitrogen at room temperature, observed with a frequency-doubled Nd:YAG laser (532 nm) at 90°, the scattering is intermediate between these two regimes and the line profile shape reflects both acoustic and thermal processes. For anisotropic molecules, the scattering is partially depolarized by molecular orientational averaging, and the central feature of the band has added to it a component of the rotational Raman scattering which corresponds to a re-orientation of the molecular spin, but no change in energy (rotational Q-branch) (Young 1982). While this component is small (less than 1% of the total scattering), its properties differ from those associated with scattering from translational motion in that it is depolarized and incoherent, even in the forward direction (in contrast to the translational motion portion where dephasing cancels out in the forward direction). Young (1981) suggests that the features associated with elastic scattering from translational motion (plus the rotational Q-branch) be called the 'Cabannes' line in honour of Lord Rayleigh's student, Jean Cabannes.

With standard lasers and unfiltered light collection, the 'Rayleigh' scattering signal is the sum of all components including the Cabannes line(s), the rotational Raman lines, and the vibrational Raman lines. Of these, the vibrational Raman scattering is so small (typically 0.1%), that its contribution can usually be neglected. Since the Cabannes 'coherent' scattering is the largest contributor, the scattered light will be strongly polarized, and the polarization direction of the laser in relation to the location of the detector can have a significant impact on the amount of light collected (Reckers *et al* 1997). Rotational Raman is usually a part of the observed signal because it falls close to the Cabannes line and is difficult to remove without a significant reduction of the Cabannes signal strength. On the other hand, strong filtering of the Cabannes line can enable the rotational Raman spectrum to be recorded (Sabbaghzadeh *et al* 1995; Finkelstein 1997a, 1998). Although rather weak, these lines are usually much stronger than the vibrational Raman lines and can be used for species and temperature measurements. Measurements based on resolving the Cabannes line profile require narrow linewidth lasers. In this case, the pressure, temperature and velocity of the gas can be determined from the scattering strength, linewidth and frequency.

'Rayleigh scattering' is used to describe scattering from molecules as well as scattering from small particles and clusters whose circumference is much less than the wavelength of the illumination light (Van de Hulst 1957). For both molecules and small particles, the induced dipole moment of the particle
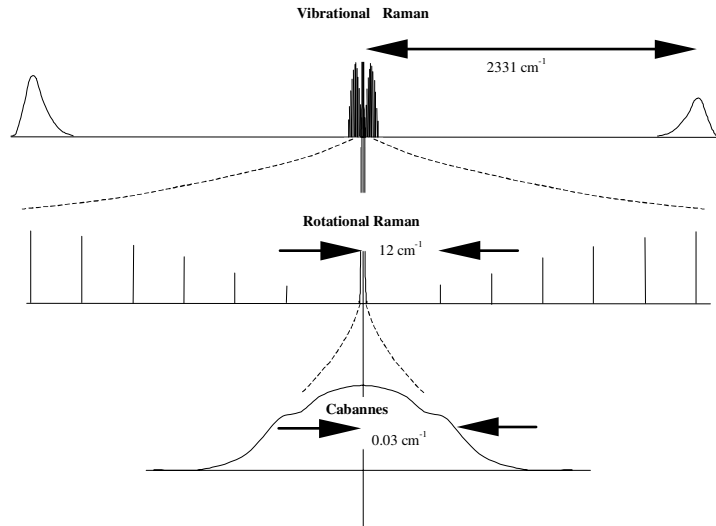
Vibrational Raman

2331 cm⁻¹

Rotational Raman

12 cm⁻¹

Cabannes

0.03 cm⁻¹

Figure 1. Scattering components from laser illumination of a diatomic molecular gas (e.g. nitrogen), at sequentially higher resolution.

is established in a time short compared to the oscillation period of the electromagnetic wave, so Rayleigh scattering is 'instantaneous' in nature. When the illumination source is turned off, Rayleigh scattering immediately ceases, in contrast to fluorescent processes where emission continues for some period of time. For small particles the thermal motion is significantly less than it is for molecules, so coherent interference from density fluctuations may persist long enough to create significant structure or 'speckle' in the collected signal.

2. Scattering cross section

2.1. Spherically symmetric model

If the molecules are spherical, such as is the case for helium, argon and other noble gases, then there is no rotational Raman scattering, and the Rayleigh scattering cross section is derived using the classical expression for radiation from an infinitesimally small oscillating dipole (Born and Wolf 1980). (Note: for a quantum mechanical formulation, see Penney 1969.) The amplitude and intensity of the electric field propagating from this dipole are shown in figure 2 and are given by

$$|\vec{E}_s(r, \phi)| = \frac{\omega^2 p \sin \phi}{4\pi r \varepsilon_0 c^2} \tag{1}$$

and

$$I_s(r, t) = \frac{\varepsilon_0 c |\vec{E}_s(r, \phi)|^2}{2} \tag{2}$$

where ω is the oscillation frequency and p is the magnitude of the oscillating dipole moment (charge times displacement) induced by the incident field. The scattering geometry is shown in figure 3, where the dipole, $\vec{p}$, is at an angle β to the vertical z-axis; ϕ is the angle of observation with respect to that dipole vector. The scattered electric field vector, $\vec{E}_s(r, \phi)$, is perpendicular to the scattering propagation vector, $\hat{0}$, and lies in the plane of the dipole vector and the scattering propagation vector. θ_x, θ_y and θ_z are the scattering angles with respect to the $\hat{x}$, $\hat{y}$ and $\hat{z}$ axes. The ω^2 term in equation (1) arises from the fact
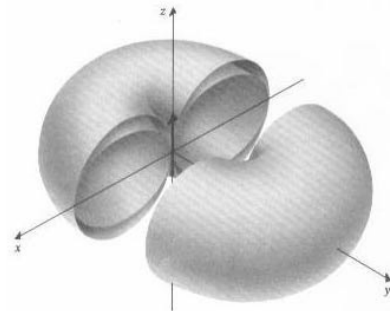

Figure 2. Polar diagram of electric (outer surface) and intensity (inner surface) field patterns around a dipole aligned with the z-axis (Long 1977). At any point on the surface, the radial distance from the origin is proportional to the magnitude of the field measured at that location.

that the radiation amplitude is proportional to the acceleration of the oscillating charge. The dipole behaves like a harmonic oscillator, so acceleration is the second time derivative of the displacement. The $\sin \phi$ dependence is a projection of the apparent dipole moment amplitude as seen from the direction of observation. When the observation position is along the axis of the dipole moment, this apparent projection goes to zero, and there is no radiated field. Non-radiating field components die out with distance faster than $1/r$, and have been neglected, which implies that the electric field is being measured many wavelengths from the dipole.

The intensity of the light scattered from a single oscillating dipole is

$$I_s = \frac{\pi^2 c p^2 \sin^2 \phi}{2\varepsilon_0 \lambda^4 r^2} \tag{3}$$

where λ is the vacuum wavelength, $\lambda = 2\pi c/\omega$.

Light scattering occurs when the dipole oscillation is driven by incident electromagnetic radiation. In the case of a spherically symmetric molecule, the dipole moment, $\vec{p}$, is induced in the same direction as the incident field polarization, and is linearly proportional to the incident electric field, $\vec{E}_I$. The scalar constant of proportionality is termed the
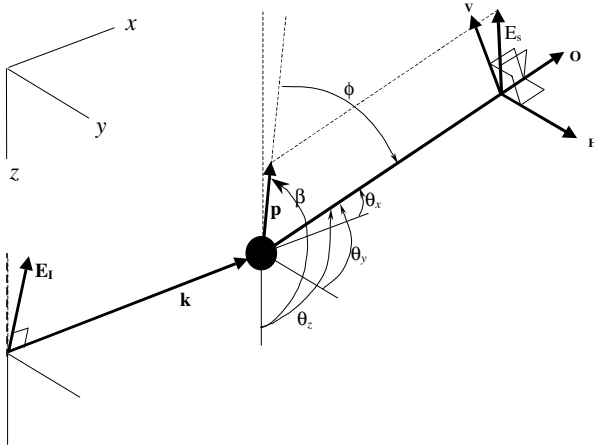
Figure 3. Rayleigh scattering geometry.

polarizability, α:

$$\vec{p} = \alpha \vec{E}_I. \tag{4}$$

By substituting $p^2 = \alpha^2 |E_I|^2$ and $I_I = (\varepsilon_0 c/2)|E_I|^2$, we find the scattering intensity from one molecule:

$$I_s = \frac{\pi^2 \alpha^2}{\varepsilon_0^2 \lambda^4 r^2} I_I \sin^2 \phi. \tag{5}$$

It is useful to define a differential scattering cross section such that

$$I_s = \frac{\partial \sigma_{ss}}{\partial \Omega} \frac{1}{r^2} I_I \tag{5a}$$

where the subscript, ss, indicates that the scattering is from a spherically symmetric scatterer and

$$\frac{\partial \sigma_{ss}}{\partial \Omega} = \frac{\pi^2 \alpha^2}{\varepsilon_0^2 \lambda^4} \sin^2 \phi. \tag{5b}$$

Integrating this intensity over the surface area of a sphere enclosing the dipole gives the total power scattered from one molecule:

$$P = \frac{8\pi^3 \alpha^2}{3\varepsilon_0^2 \lambda^4} I_I. \tag{6}$$

The total scattered power is often written in terms of a total scattering cross section:

$$\sigma_{ss} = \frac{P}{I_I} \tag{7}$$

or

$$\sigma_{ss} = \frac{8\pi^3 \alpha^2}{3\varepsilon_0^2 \lambda^4}. \tag{8}$$

The polarizability can be related to the index of refraction, n, by the Lorentz–Lorenz equation (Born and Wolf 1980):

$$\alpha = \frac{3\varepsilon_0}{N} \frac{n^2 - 1}{n^2 + 2} \tag{9}$$

where N is the number density of the gas (molecules m^{-3}), so the scattering cross section of a spherically symmetric scatterer can be written

$$\sigma_{ss} = \frac{24\pi^3}{\lambda^4 N^2} \left(\frac{n^2 - 1}{n^2 + 2} \right)^2 \tag{9a}$$

Note that $(1/N)[(n^2 - 1)/(n^2 + 2)]$ is independent of density, as required for α to be a property of the individual atom or molecule. $3/(n^2 + 2)$ is a field correction factor, which is generally valid for gases, and is approximately valid for liquids and solids (Jackson 1998). For the atmosphere and other low density gases, the index of refraction is usually close to 1 (in air the index of refraction is 1.000 278 at 530 nm), so the total cross section can be approximated

$$\sigma_{ss} \cong \frac{32\pi^3}{3\lambda^4} \left(\frac{n-1}{N} \right)^2 \tag{10}$$

and the differential cross section is

$$\frac{\partial \sigma_{ss}}{\partial \Omega} \cong \frac{4\pi^2}{\lambda^4} \left(\frac{n-1}{N} \right)^2 \sin^2 \phi. \tag{11}$$

When Rayleigh scattering is used for diagnostics, the scattered light is collected over a limited solid angle which is usually determined by a collection lens. In that case the power collected is derived from the differential cross section

$$\partial P = \frac{\partial \sigma_{ss}}{\partial \Omega} I_I \partial \Omega \tag{12}$$

integrated over the collection solid angle, $\Delta\Omega$. This yields the collected power

$$\Delta P = I_I \int_{\Delta\Omega} \frac{\partial \sigma_{ss}}{\partial \Omega} \partial \Omega. \tag{13}$$

The motion of the molecules randomizes the interference of the electric fields scattered from each individual molecule so that, when seen from afar, these coherent effects cancel and the total scattering becomes the sum of the individual intensities scattered from each molecule. The total power that is collected is the integral of the differential cross section over the solid angle subtended by the collection optics, $\Delta\Omega$, multiplied by the number of scatterers in the observation volume, NV, and further multiplied by whatever efficiencies, η, are appropriate for the optical elements and the detector:

$$P_{DET} = \eta I_I N V \int_{\Delta\Omega} \frac{\partial \sigma_{ss}}{\partial \Omega} \mathrm{d}\Omega. \tag{14}$$

The polarization of the scattered light is determined by the polarization of the dipole and the viewing angle. In the case of spherically symmetric scatterers, the dipole is polarized in the same direction as the polarization of the incident field. If the incident field is assumed to propagate along the x-axis, then one may choose the direction of polarization to be along the z-axis. The polarization of the scattered light must project onto that dipole, $\vec{p}$, and be orthogonal to the propagation direction, $\hat{0}$, i.e., it must lie in the $\hat{0}$–$\hat{z}$-plane if $\vec{p}$ is in the z-direction. Scattering observed along the z-axis has zero amplitude since there is no polarization component perpendicular to z, or equivalently, $\sin\phi = 0$. If the incident light is randomly polarized, then an induced polarization in the direction of the y-axis occurs and the scattered light has a polarization component in the $\hat{0}$–$\hat{y}$-plane.

2.2. Scattering from diatomic molecules

Scattering from molecules is more complicated because, in general, molecules are not spherical. Rotational Raman lines appear, and the Rayleigh scattering is slightly depolarized since the induced dipole moment is not necessarily in the direction of the applied field. The random orientation of the molecule with respect to the incident field, and with respect to the observation direction and observed polarization, leads to the requirement that the scattering model include averaging over the molecular orientations.

If we assume that the incident laser field is propagating in the x-direction, then it can have only two polarization components, E_y and E_z, since propagating light must have an electric field polarization orthogonal to the propagation direction. The induced electric dipole moment, $\vec{p}$, is described by a dipole polarizability tensor whose components are, therefore:

$$p_x = \alpha_{xy}E_{Iy} + \alpha_{xz}E_{Iz}$$

$$p_y = \alpha_{yy}E_{Iy} + \alpha_{yz}E_{Iz}$$

$$p_z = \alpha_{zy}E_{Iy} + \alpha_{zz}E_{Iz}. \tag{15}$$

Note that all components of dipole moment orientation are now allowed.

The electric field polarization of the light emitted by the oscillating dipole must be co-planar with the dipole moment vector of the molecule. Using figure 3 as a reference, if z is 'down', then 'horizontally' polarized scattering is defined to be parallel to the $x-y$-plane and will lie along the unit vector $\hat{H}$. The orthogonal scattering component, $\hat{V}$, is perpendicular to both this horizontal polarization and to the propagation direction, and will intersect (or be parallel to) the z-axis. (This geometry assumes that the observation direction is not along the z-axis, in which case the definition of horizontal polarization becomes ambiguous.) The V component always has a non-zero projection on the z-axis, as contrasted with the H component, that is always orthogonal to z. For convenience, therefore, we call V the 'vertical' scattering component. With these definitions, the horizontal and vertical polarization directions can be written in terms of scattering propagation angle cosines as follows:

$$H_x = \frac{\cos\theta_y}{\sqrt{\cos^2\theta_x + \cos^2\theta_y}}$$

$$H_y = \frac{-\cos\theta_x}{\sqrt{\cos^2\theta_x + \cos^2\theta_y}} \qquad H_z = 0 \tag{16}$$

$$V_x = \frac{\cos\theta_x \cos\theta_z}{\sqrt{\cos^2\theta_x + \cos^2\theta_y}} \qquad V_y = \frac{\cos\theta_y \cos\theta_z}{\sqrt{\cos^2\theta_x + \cos^2\theta_y}}$$

$$V_z = -\sqrt{\cos^2\theta_x + \cos^2\theta_y} \tag{17}$$

where the propagation vector of the scattered light is expressed:

$$\hat{0} = \cos\theta_x \hat{x} + \cos\theta_y \hat{y} + \cos\theta_z \hat{z}. \tag{18}$$

$\hat{H}$ and $\hat{V}$ are normalized and oriented so the following relations are satisfied:

$$\hat{V} \cdot \hat{V} = 1 \qquad \hat{H} \cdot \hat{H} = 1 \qquad \hat{H} \cdot \hat{V} = 0$$

$$\hat{H} \cdot \hat{0} = 0 \qquad \hat{V} \cdot \hat{0} = 0.$$

The 'vertical' and horizontal components of the scattering intensity arise from the 'vertical' and horizontal components of the dipole moment vector, so

$$I_v = \frac{\pi^2 c}{2\varepsilon_0 \lambda^4 r^2} |\vec{p} \cdot \hat{V}|^2 \tag{19}$$

and

$$I_H = \frac{\pi^2 c}{2\varepsilon_0 \lambda^4 r^2} |\vec{p} \cdot \hat{H}|^2. \tag{20}$$

From these relations we obtain the expression for the vertical and horizontal polarizations of the scattered intensity from a single molecule.

$$I_V = K\left[p_x^2 \frac{\cos^2\theta_x \cos^2\theta_z}{(\cos^2\theta_x + \cos^2\theta_y)} + p_y^2 \frac{\cos^2\theta_y \cos^2\theta_z}{(\cos^2\theta_x + \cos^2\theta_y)} \right.$$
$$+ p_z^2(\cos^2\theta_x + \cos^2\theta_y) + 2p_x p_y \frac{\cos\theta_x \cos\theta_y \cos^2\theta_z}{(\cos^2\theta_x + \cos^2\theta_y)}$$
$$\left. - 2p_y p_z \cos\theta_y \cos\theta_z - 2p_z p_x \cos\theta_z \cos\theta_x \right] \tag{21}$$

and

$$I_H = K\left[p_x^2 \frac{\cos^2\theta_y}{(\cos^2\theta_x + \cos^2\theta_y)} + p_y^2 \frac{\cos^2\theta_x}{(\cos^2\theta_x + \cos^2\theta_y)} \right.$$
$$\left. - 2p_x p_y \frac{\cos\theta_x \cos\theta_y}{(\cos^2\theta_x + \cos^2\theta_y)} \right] \tag{22}$$

where

$$K = \frac{\pi^2 c}{2\varepsilon_0 \lambda^4 r^2}.$$

When these are summed together, the expression for the total scattered intensity, equation (3), is recovered using the fact that

$$(p\sin\phi)^2 = p^2 - (p\cos\phi)^2 = p^2 - (\vec{p} \cdot \hat{0})^2$$
$$= p^2 - (p_x \cos\theta_x + p_y \cos\theta_y + p_z \cos\theta_z)^2$$

and the relations

$$p^2 = p_x^2 + p_y^2 + p_z^2 \qquad \text{and} \qquad \cos^2\theta_x + \cos^2\theta_y + \cos^2\theta_z = 1.$$

3. Orientation averaging

Since the molecules in the sample volume are randomly oriented, the scattering must be averaged over all molecular angles. This averaging can be expressed in terms of two parameters which are invariant with respect to rotation: the mean polarizability, a, and the anisotropy, γ.

$$a^2 = \frac{1}{9}(\alpha_{\underline{xx}} + \alpha_{\underline{yy}} + \alpha_{\underline{zz}})^2 \tag{23}$$

$$\gamma^2 = \frac{1}{2}\{(\alpha_{\underline{xx}} - \alpha_{\underline{yy}})^2 + (\alpha_{\underline{yy}} - \alpha_{\underline{zz}})^2 + (\alpha_{\underline{zz}} - \alpha_{\underline{xx}})^2$$
$$+ 6(\alpha_{\underline{xy}}^2 + \alpha_{\underline{yz}}^2 + \alpha_{\underline{zx}}^2)\} \tag{24}$$

where $\underline{x}$, $\underline{y}$ and $\underline{z}$ are in the molecular frame, but not necessarily along the molecular axis.

In terms of these invariant quantities, the orientationally averaged polarizabilities are (Long 1977)

$$\overline{\alpha_{\underline{xx}}^2} = \overline{\alpha_{\underline{yy}}^2} = \overline{\alpha_{\underline{zz}}^2} = \frac{45a^2 + 4\gamma^2}{45} \tag{25}$$

$$\overline{\alpha_{\underline{xy}}^2} = \overline{\alpha_{\underline{xz}}^2} = \overline{\alpha_{\underline{yx}}^2} = \overline{\alpha_{\underline{yz}}^2} = \overline{\alpha_{\underline{zx}}^2} = \overline{\alpha_{\underline{zy}}^2} = \frac{\gamma^2}{15} \tag{26}$$

$$\overline{\alpha_{xx}\alpha_{yy}} = \overline{\alpha_{yy}\alpha_{zz}} = \overline{\alpha_{zz}\alpha_{xx}} = \frac{45a^2 - 2\gamma^2}{45} \quad (27)$$

$$\overline{\alpha_{xy}\alpha_{xz}} = \overline{\alpha_{yz}\alpha_{xy}} = \overline{\alpha_{xz}\alpha_{yz}} = 0. \quad (28)$$

In the case of diatomic and linear molecules, there is cylindrical symmetry and the invariant parameters become

$$a^2 = \tfrac{1}{9}(\alpha_{\underline{XX}} + 2\alpha_{\underline{YY}})^2 \quad (29)$$

$$\gamma^2 = (\alpha_{\underline{XX}} - \alpha_{\underline{YY}})^2 \quad (30)$$

where $\underline{X}$ is the axis of symmetry of the molecule, $\underline{Y}$ and $\underline{Z}$ are normal to it and the polarizabilities in the $\underline{Y}$ and $\underline{Z}$ directions are equal.

The expressions derived in the previous section are in terms of the components of the dipole moment vector. If β is defined as the angle between the z-axis and the incident field polarization direction, then the incident field components are

$$E_{Iy} = E_I \sin \beta \qquad E_{Iz} = E_I \cos \beta \quad (31)$$

since the incident laser propagates in the x-direction and, therefore, has no electric field component in that direction. The average of the relevant components of the dipole moment vector then are found by substitution from equation (15):

$$\overline{p_x^2} = \overline{\alpha_{xy}^2}E_{I_y}^2 + 2\overline{\alpha_{xy}\alpha_{xz}}E_{I_y}E_{I_z} + \overline{\alpha_{xz}^2}E_{I_x}^2 = E_I^2\frac{3\gamma^2}{45}. \quad (32)$$

Similarly

$$\overline{p_y^2} = E_I^2\left[\frac{3\gamma^2}{45} + \sin^2\beta\left(\frac{45a^2 + \gamma^2}{45}\right)\right] \quad (33)$$

$$\overline{p_z^2} = E_I^2\left[\frac{3\gamma^2}{45} + \cos^2\beta\left(\frac{45a^2 + \gamma^2}{45}\right)\right] \quad (34)$$

$$\overline{p_x p_y} = 0 \quad (35)$$

$$\overline{p_y p_z} = E_I^2 \sin\beta\cos\beta\left(\frac{45a^2 + \gamma^2}{45}\right) \quad (36)$$

$$\overline{p_z p_x} = 0. \quad (37)$$

Substituting these into equations (21) and (22) gives the horizontal and vertical components of the scattering intensity, assuming linearly polarized laser illumination polarized at an angle, β, to the z-axis and detection at angles θ_x, θ_y and θ_z from the respective x, y and z axes. These expressions are best written as differential cross sections (E_I^2 is replaced by $2I_I/c\varepsilon_0$, and then the intensity and $1/r^2$ terms are factored out).

$$\frac{\partial^\beta \sigma_V}{\partial\Omega} = C\left[\left(\frac{3\gamma^2}{45}\right) + \left(\frac{45a^2 + \gamma^2}{45}\right)\left(\sin\beta\frac{\cos\theta_y\cos\theta_z}{\sin\theta_z}\right.\right.$$
$$\left.\left. - \cos\beta\sin\theta_z\right)^2\right] \quad (38)$$

$$\frac{\partial^\beta \sigma_H}{\partial\Omega} = C\left[\left(\frac{3\gamma^2}{45}\right) + \left(\frac{45a^2 + \gamma^2}{45}\right)(\sin\beta)\right.$$
$$\left. \times\left(\frac{\sin^2\theta_z - \cos^2\theta_y}{\sin^2\theta_z}\right)\right] \quad (39)$$

where $C = \pi^2/\varepsilon_0^2\lambda^4$, and the superscript β indicates that the incident field is polarized at an angle β to the vertical, downward pointing z-axis.

By summing these two cross sections and simplifying, an expression for the total differential scattering cross section is found:

$$\frac{\partial^\beta \sigma_0}{\partial\Omega} = C\left[\left(\frac{45a^2 + 7\gamma^2}{45}\right)\right.$$
$$\left. -\left(\frac{45a^2 + \gamma^2}{45}\right)(\sin\beta\cos\theta_y + \cos\beta\cos\theta_z)^2\right] \quad (40)$$

where the subscript 0 indicates that the detector collects all polarizations. Note that symmetry in the x-direction allows the elimination of θ_x as a parameter (it is implicit, given θ_y and θ_z). The total Rayleigh scattering cross section is found by integrating the total differential scattering cross section over 4π steradians:

$$\sigma = \left(\frac{8\pi^3}{3\varepsilon_0^2\lambda^4}\right)\left(\frac{45a^2 + 10\gamma^2}{45}\right) \quad (41)$$

Except for the addition of the anisotropy factor, this total scattering cross section is the same as that of a spherically symmetric molecule (equation (8)). The anisotropy factor can be seen as arising from the rotational Raman components, as will be further discussed in the following section. The scattering for unpolarized incident light is found by averaging the differential scattering components in equations (38)–(40) over all possible values of beta from zero to π. This average yields

$$\frac{\partial^0 \sigma_V}{\partial\Omega} = C\left[\left(\frac{3\gamma^2}{45}\right) + \left(\frac{45a^2 + \gamma^2}{90}\right)\right.$$
$$\left. \times\left(\frac{\cos^2\theta_y\cos^2\theta_z}{\sin^2\theta_z} + \sin^2\theta_z\right)\right] \quad (42)$$

$$\frac{\partial^0 \sigma_H}{\partial\Omega} = C\left[\left(\frac{3\gamma^2}{45}\right) + \left(\frac{45a^2 + \gamma^2}{90}\right)\left(\frac{\sin^2\theta_z - \cos^2\theta_y}{\sin^2\theta_z}\right)\right] \quad (43)$$

where the superscript 0 indicates unpolarized incident light. The sum of these two components gives

$$\frac{\partial^0 \sigma_0}{\partial\Omega} = C\left[\left(\frac{45a^2 + 7\gamma^2}{45}\right)\right.$$
$$\left. -\left(\frac{45a^2 + \gamma^2}{90}\right)(\cos^2\theta_y + \cos^2\theta_z)\right]. \quad (44)$$

Equation (44), when integrated over 4π steradians, gives the same total cross section as in equation (41).

These expressions are often written in terms of ρ_0, which is defined to be the ratio of the horizontally-to-vertically polarized light scattered at $90°$ for unpolarized (natural) incident light propagating along the x-axis—i.e. parallel to the horizontal plane.

$$\rho_0 = \frac{6\gamma^2}{45a^2 + 7\gamma^2}. \quad (45)$$

Note that for a spherically symmetric molecule, there can be no induced polarization along the propagation direction of the incident light, so the scattered light must contain no horizontal component, and ρ_0 is zero.

The mean polarizability also leads to the index of refraction of the molecular gas, so the Lorentz–Lorenz relation (equation (9)) can be used together with the approximation

Table 1. (Forkey 1996). Total and differential scattering cross sections for incident light along the x-axis, and arbitrary observation direction not along the z-axis (given by θ_x, θ_y and θ_z). Natural, unpolarized incident light corresponds to equations with superscript 0; linearly polarized incident light corresponds to equations with superscript β, where β indicates the polarization direction relative to the z-axis. Subscripts V and H correspond to detection of vertically or horizontally polarized light, and subscript 0 corresponds to polarization insensitive detection.

$$\sigma = \frac{32\pi^3(n-1)^2}{3\lambda^4 N^2}\left(\frac{6+3\rho_0}{6-7\rho_0}\right) \tag{1.1}$$

$$\frac{\partial^\beta \sigma_V}{\partial \Omega} = \frac{3\sigma}{8\pi}\frac{1}{2+\rho_0}\left[\rho_0 + (2-2\rho_0)\left(\sin\beta\frac{\cos\theta_y\cos\theta_z}{\sin\theta_z} - \cos\beta\sin\theta_z\right)^2\right] \tag{1.2}$$

$$\frac{\partial^\beta \sigma_H}{\partial \Omega} = \frac{3\sigma}{8\pi}\frac{1}{2+\rho_0}\left[\rho_0 + (2-2\rho_0)(\sin^2\beta)\left(\frac{\sin^2\theta_z - \cos^2\theta_y}{\sin^2\theta_z}\right)\right] \tag{1.3}$$

$$\frac{\partial^\beta \sigma_0}{\partial \Omega} = \frac{3\sigma}{8\pi}\frac{1}{2+\rho_0}[2 - (2-2\rho_0)(\sin\beta\cos\theta_y + \cos\beta\cos\theta_z)^2] \tag{1.4}$$

$$\frac{\partial^0 \sigma_V}{\partial \Omega} = \frac{3\sigma}{8\pi}\frac{1}{2+\rho_0}\left[\rho_0 + (1-\rho_0)\left(\frac{\cos^2\theta_y\cos^2\theta_z}{\sin^2\theta_z} + \sin^2\theta_z\right)\right] \tag{1.5}$$

$$\frac{\partial^0 \sigma_H}{\partial \Omega} = \frac{3\sigma}{8\pi}\frac{1}{2+\rho_0}\left[\rho_0 + (1-\rho_0)\left(\frac{\sin^2\theta_z - \cos^2\theta_y}{\sin^2\theta_z}\right)\right] \tag{1.6}$$

$$\frac{\partial^0 \sigma_0}{\partial \Omega} = \frac{3\sigma}{8\pi}\frac{1}{2+\rho_0}[2 - (1-\rho_0)(\cos^2\theta_y + \cos^2\theta_z)] \tag{1.7}$$

$n \cong 1$ to obtain $a^2 = 4\varepsilon_0^2[(n-1)/N]^2$. By solving the above expression for γ and substituting into equation (41), the total cross section becomes

$$\sigma = \sigma_{ss}\left(\frac{6+3\rho_0}{6-7\rho_0}\right) = \sigma_{ss}\left(1 + \frac{10}{45}\frac{\gamma^2}{a^2}\right). \tag{46}$$

Cavity-ringdown experiments have recently been used to verify this cross section for N_2, Ar and SF_6 (Naus and Ubachs 2000). Equations for the differential cross sections for polarized (angle β to z-axis) and unpolarized incident light are given in table 1.

The ratio $((6+3\rho_0)/(6-7\rho_0))$ is often called the 'King correction factor'. Table 2 gives the effective King correction factors, which approximate air as a single species (Bates 1984), and recently updated Rayleigh scattering cross sections (Bucholtz 1995). This table is based on a four parameter fit for the index of refraction of air for wavelengths greater than 0.23 μm (Bucholtz 1995):

$$(n_x - 1) \times 10^8 = \frac{5\,791\,817}{238.0185 - (1/\lambda)^2} + \frac{167\,909}{57.362 - (1/\lambda)^2}$$
$$\lambda > 0.23\ \mu\text{m} \tag{47}$$

and a five parameter fit for wavelengths less than or equal to 0.23 μm

$$(n_x - 1) \times 10^8 = 8060.51 + \frac{2\,480\,990}{132.274 - (1/\lambda)^2}$$
$$+\frac{17\,455.7}{39.329\,57 - (1/\lambda)^2} \qquad \lambda < 0.23\ \mu\text{m} \tag{48}$$

where λ is in micrometres and the air is at 288.15 K and 1013.25 mbar.

In the case of linearly polarized laser illumination propagating along the x-axis, the z-axis can be defined to lie along the polarization direction. The scattering is then only a function of the angle of observation measured from the z-axis, and the equations simplify to those shown in table 3, with the 'horizontal' component interpreted to mean the component of the scattering orthogonal to the z-axis. For many experiments, the laser propagates along the x-axis, is polarized along the z-axis and light is collected at 90° along the y-axis. Under those conditions

$$\frac{\partial \sigma_V}{\partial \Omega} = \frac{3\sigma}{8\pi}\left(\frac{2-\rho_0}{2+\rho_0}\right) \tag{49}$$

$$\frac{\partial \sigma_H}{\partial \Omega} = \frac{3\sigma}{8\pi}\frac{\rho_0}{2+\rho_0}. \tag{50}$$

4. Rayleigh density measurements in molecular gases

Rayleigh scattering can be used to measure density and density fluctuations, since the signal is linearly proportional to the number of scatterers. As noted below, the scattering from small particles can easily dominate molecular scattering, so for experiments where the density of a molecular gas is desired, either spectral filtering is required, or the experimental region must be dust free. Flow fields can be imaged with a single laser pulse by using a molecular gas with a large scattering cross section such as freon (Escoda and Long 1983), by using a very high energy laser system (Long et al 1985), or with ultraviolet lasers (Dam et al 1998). Note that in the ultraviolet, the Rayleigh scattering cross section is significantly increased both by the frequency to the fourth power scaling and by resonance enhancement from nearby electronic transitions (Stanton and Pecora 1981). If the pressure is known, then the density can be used to determine the temperature using the ideal gas law (Pitz et al 1976, Dibble and Hollenbach 1981). An example of instantaneous and time averaged Rayleigh images taken with a pulsed ultraviolet laser of an overexpanded supersonic free jet are shown in figure 4. Atmospheric density LIDAR profiles have also been taken using Rayleigh scattering from a pulsed laser collected with a large aperture mirror (Sica 1995). In this

Table 2. List of wavelengths, refractive indices, Rayleigh scattering cross sections and effective King correction factor for standard air (288.15 K, 1013.25 mbar) (Bates 1984, Bucholtz 1995).

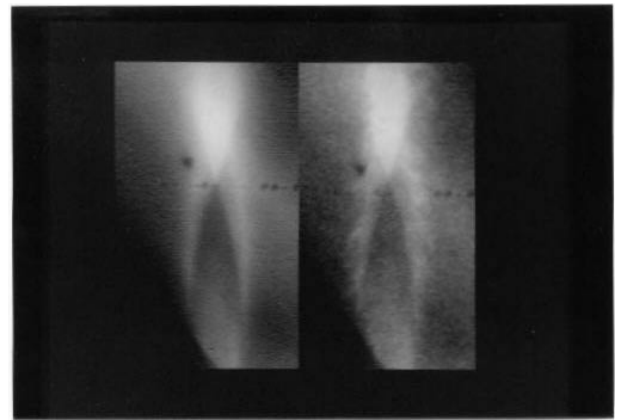| Wavelength (μm)	F_k (air) $\left(\dfrac{6+3\rho_0}{6-7\rho_0}\right)$	Refractive index in air $(n-1) \times 10^4$	Rayleigh-scattering cross section σ (cm^2)
0.200	1.080	3.2378	3.612 ($\times 10^{-25}$)
0.210	1.074	3.1737	2.836
0.220	1.070	3.1222	2.269
0.230	1.066	3.0799	1.841
0.240	1.064	3.0445	1.515
0.250	1.062	3.0146	1.259
0.260	1.060	2.9890	1.056
0.270	1.059	2.9669	8.939 ($\times 10^{-26}$)
0.280	1.057	2.9475	7.614
0.290	1.056	2.9306	6.534
0.300	1.055	2.9155	5.642
0.310	1.055	2.9022	4.903
0.320	1.054	2.8902	4.279
0.330	1.053	2.8795	3,752
0.340	1.053	2.8698	3.307
0.350	1.052	2.8611	2.924
0.360	1.052	2.8531	2.598
0.370	1.052	2.8458	2.317
0.380	1.051	2.8392	2.071
0.390	1.051	2.8331	1.858
0.400	1.051	2.8275	1.673
0.410		2.8223	1.509
0.420		2.8175	1.366
0.430		2.8131	1.239
0.440		2.8090	1.127
0.450	1.050	2.8052	1.027
0.460		2.8016	9.378 ($\times 10^{-27}$)
0.470		2.7983	8.583
0.480		2.7952	7.871
0.490		2.7923	7.232
0.500	1.049	2.7896	6.656 ($\times 10^{-27}$)
0.510		2.7870	6.138
0.520		2.7846	5.669
0.530		2.7824	5.245
0.540		2.7803	4.860
0.550	1.049	2.7782	4.509
0.560		2.7763	4.189
0.570		2.7745	3.897
0.580		2.7728	3.630
0.590		2.7712	3.385
0.600	1.048	2.7697	3.161
0.610		2.7682	2.956
0.620		2.7669	2.767
0.630		2.7656	2.593
0.640		2.7643	2.432
0.650	1.048	2.7631	2.284
0.660		2.7620	2.147
0.670		2.7609	2.020
0.680		2.7599	1.903
0.690		2.7589	1.793
0.700	1.048	2.7579	1.692
0.710		2.7570	1.597
0.720		2.7562	1.510
0.730		2.7553	1.428
0.740		2.7545	1.351
0.750	1.048	2.7538	1.280
0.760		2.7530	1.213
0.770		2.7523	1.150
0.780		2.7516	1.092
0.790		2.7510	1.037
0.800	1.047	2.7504	9.854 ($\times 10^{-28}$)
0.850	1.047	2.7476	

Table 2. (Continued)

Wavelength (μm)	F_k (air) $\left(\dfrac{6+3\rho_0}{6-7\rho_0}\right)$	Refractive index in air $(n-1) \times 10^4$	Rayleigh-scattering cross section σ (cm^2)
0.900	1.047	2.7452	6.129
0.950	1.047	2.7432	
1.000	1.047	2.7416	4.010

Table 3. (Forkey 1996). Differential scattering cross sections for linearly polarized incident light propagating along the x-axis, and arbitrary observation direction not along the z-axis (given by θ_x, θ_y and θ_z). The polarization direction of the incident light is assumed to be oriented along the z-axis.

$$\frac{\partial^{\beta=0}\sigma_v}{\partial\Omega} = \frac{3\sigma}{8\pi}\frac{1}{2+\rho_0}[\rho_0 + (2-2\rho_0)(1-\cos^2\theta_z)] \quad (3.1)$$

$$\frac{\partial^{\beta=0}\sigma_H}{\partial\Omega} = \frac{3\sigma}{8\pi}\frac{1}{2+\rho_0}\rho_0 \quad (3.2)$$

$$\frac{\partial^{\beta=0}\sigma_0}{\partial\Omega} = \frac{3\sigma}{8\pi}\frac{1}{2+\rho_0}[2-(2-2\rho_0)(\cos^2\theta_z)] \quad (3.3)$$

Figure 4. Ultraviolet Rayleigh images of an overexpanded supersonic nitrogen jet. The left image is time averaged and the right image is instantaneous.

case the signal was time gated to collect only the return from the 30 to 100 km altitude range, so scattering was predominantly for air molecules and aerosols did not contaminate the signal.

The low power of a continuous laser usually limits Rayleigh scattering measurements with that type of laser to a single point, but the time variation of the signal from that point can be used to measure fluctuating flow parameters related to such phenomena as turbulence or acoustic noise generation. The location of the point can be moved to obtain field measurements. For example, Rayleigh scattering has been used to observe density effects in free jets for the study of turbulence at subsonic speeds (Richards and Pitts 1993) and screech noise generation in supersonic flows (Panda and Seasholtz 1999). In both these cases, illumination has been with an argon ion laser, and great care has been taken to remove particles from the flow and to include proper light baffling to avoid contributions to the signal from background scattering. Illumination was at 90°, and no polarization discrimination was used. In the supersonic experiments, the observation point was
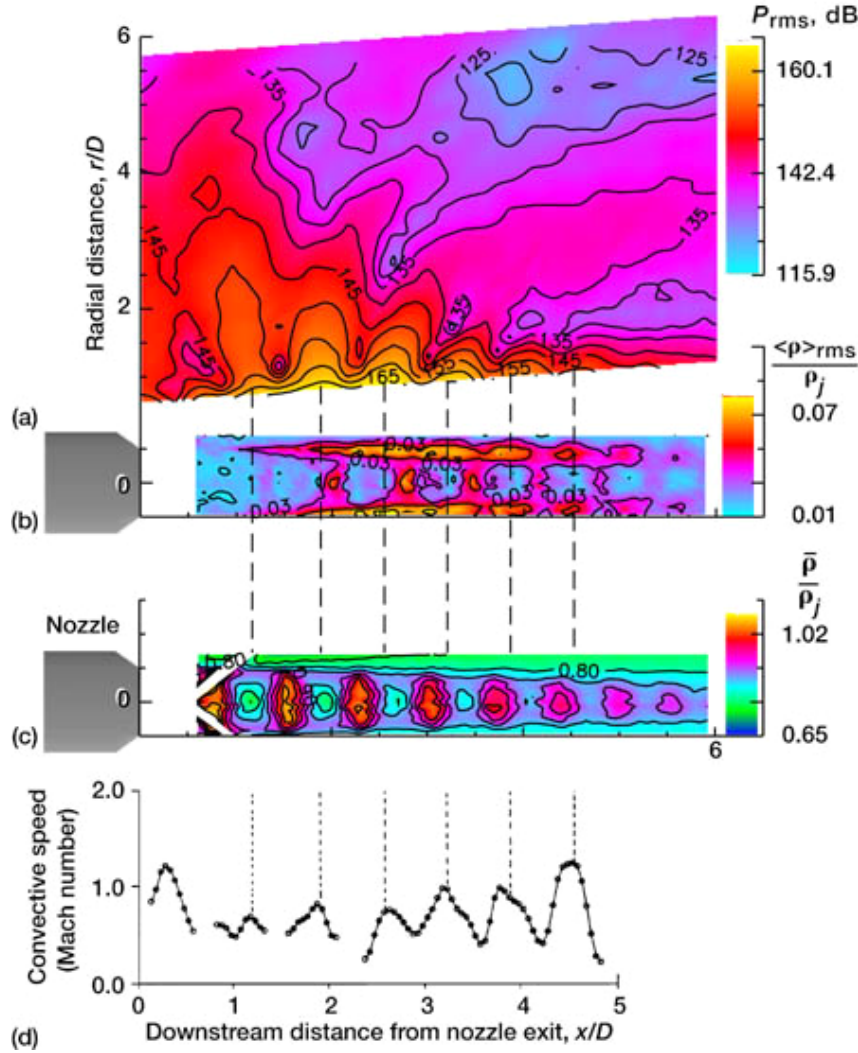
Figure 5. Screech generation from an underexpanded Mach 1.19 air jet. Image (a) is the pressure field associated with the screech measured outside of the jet, (b) is the Rayleigh measurement of density fluctuations in the jet, (c) is the Rayleigh measurement of time averaged density in the jet and (d) is the centreline Mach number. (Panda and Seasholtz 1999.)

moved to obtain the time averaged density and coherent density fluctuation fields. Figure 5 is taken from those experiments and shows the density and density fluctuation fields downstream of the nozzle exit of a Mach 1.19 jet. In the region outside the jet, the noise field was measured and correlated with the density fluctuations to indicate the noise generating regions.

5. Rayleigh scattering spectral components

It is important to note that the differential scattering cross sections have been derived independent of the rotational or translational motion of the molecules. If the molecules are free to rotate, the averaging process leads to constant terms as well as to terms that have the form $\cos[2\pi(2\nu_R t)]$, where ν_R is the rotation frequency. This light corresponds to rotational Raman scattering, the magnitude of which is included in the total and differential Rayleigh scattering cross sections. Rotational Raman consists of three branches, the Stokes and anti-Stokes rotational branches that are spectrally shifted away from the illumination frequency, and the Raman Q-branch which is

unshifted in frequency. The Raman Q-branch corresponds to no change of the rotational state, $\Delta J = 0$, but to changes of the m_J states of the molecule, $\Delta m_J = \pm 2$. The m_J states are projections of the rotation moment onto the molecular axis, so a change in m_J corresponds to a reorientation of the molecule, but no change in energy. Since Raman scattering leads to a change of the molecular state, the Raman light scattered is incoherent, even in the forward direction. The unshifted Raman scattering is part of the Cabannes line and adds to the coherent component, which Young calls the Placzek 'trace scattering' (Young 1982). This Placzek scattering is frequency shifted by molecular motion, but not by the internal degrees of freedom of the molecule itself. There are, therefore, three separate components to the Rayleigh scattering cross section for a single species gas: the Placzek trace scattering, the rotational Raman Q-branch, and the rotational Raman Stokes and anti-Stokes branches. The relative magnitudes of these components have been tabulated by Kattawar *et al* (1981) for the case of scattering detected in the x–y-plane, and the polarization ratios have been confirmed by experiment (Rowell and Aval 1971). These magnitudes are shown in table 4,

Table 4. Three components of the Rayleigh scattering cross section for a single species gas for scattering detected in the x, y plane: the Placzek trace scattering (single prime), the rotational Raman Q-branch (double prime), and the rotational Raman Stokes and anti-Stokes branches (triple prime). H or V superscripts refer to the input light and the H or V subscripts refer to the collected light (from Kattawar *et al* 1981).

	Vertically polarized input light	Horizontally polarized input light
Cabannes line (coherent portion (polarized) or Placzek scattering	$^V K_V' = 180$ $^V K_H' = 0$ $^V K_0' = 180$	$^H K_V' = 0$ $^H K_H' = 180\cos^2\theta$ $^H K_0' = 180\cos^2\theta$
Q-branch rotational Raman (incoherent portion of Cabannes line (unpolarized)	$^V K_V'' = 4\varepsilon$ $^V K_H'' = 3\varepsilon$ $^V K_0'' = 7\varepsilon$	$^H K_V'' = 3\varepsilon$ $^H K_H'' = 3\varepsilon + \varepsilon\cos^2\theta$ $^H K_0'' = 6\varepsilon + \varepsilon\cos^2\theta$
Stokes/anti-Stokes rotational Raman (unpolarized) (incoherent)	$^V K_V''' = 12\varepsilon$ $^V K_H''' = 9\varepsilon$ $^V K_0''' = 21\varepsilon$	$^H K_V''' = 9\varepsilon$ $^H K_H''' = 9\varepsilon + 3\varepsilon\cos^2\theta$ $^H K_0''' = 18\varepsilon + 3\varepsilon\cos^2\theta$
Total scattering	$^V T_V = 180 + 16\varepsilon$ $^V T_H = 12\varepsilon$ $^V T_0 = 180 + 28\varepsilon$	$^H T_V = 12\varepsilon$ $^H T_H = 12\varepsilon + (180 + 4\varepsilon)\cos^2\theta$ $^H T_0 = 24\varepsilon + (180 + 4\varepsilon)\cos^2\theta$

where θ is the scattering angle measured from the propagation direction of the incident beam ($\theta = \theta_x$ for light observed in the x–y-plane and an incident beam along the x-axis).

In the table, ε is equal to γ^2/a^2, which may be related to ρ_0 by the expression

$$\varepsilon = \frac{45\rho_0}{6 - 7\rho_0}. \tag{51}$$

From these relative magnitudes, the differential scattering cross sections for each of the scattering components are found and are summarized in table 5 for observation in the x–y-plane where the index, j, refers to whichever component is to be found (j is a single, double, or triple prime corresponding to the notation in table 4). These expressions can be generalized to naturally occurring or unpolarized light by letting $\beta = \pi/4$, i.e., ($\cos^2\beta = \sin^2\beta = 1/2$).

In the case where light is detected with a polarization insensitive detector in the x–y-plane, with the incident polarization vector lying in the z–y-plane (as it must for light propagating in the x-direction), differential scattering cross sections become

$$\frac{\partial^\beta \sigma_0}{\partial\Omega} = \frac{\sigma}{8\pi}\frac{6 - 7\rho_0}{2 + \rho_0}\sin^2\phi \tag{52}$$

Cabannes line coherent (Placzek) component

$$\frac{\partial^\beta \sigma_0}{\partial\Omega} = \frac{\sigma}{32\pi}\frac{\rho_0}{2 + \rho_0}(6 + \sin^2\phi) \tag{53}$$

Cabannes line incoherent component

$$\frac{\partial^\beta \sigma_0}{\partial\Omega} = \frac{3\sigma}{32\pi}\frac{\rho_0}{2 + \rho_0}(6 + \sin^2\phi) \qquad \text{rotational Raman} \tag{54}$$

for the Placzek trace scattering, the Q-branch rotational Raman scattering and the Stokes/anti-Stokes rotational Raman scattering, respectively. ϕ is the angle between the observation direction and the polarization direction of the incident field. ϕ is related to β and θ by the expression $\sin^2\phi = 1 - \sin^2\beta\sin^2\theta$. Note that the Placzek trace scattering just reduces to the scattering from a spherically symmetric scatterer, $\partial\sigma_{ss}/\partial\Omega$, as expressed in equation (11).

The depolarization of the Cabannes line can be used to detect molecular concentrations in the presence of atomic species such as for measurements of molecules in plasmas (Meulenbroeks *et al* 1992). In the forward direction ($\theta = 0$), the Placzek coherent component of the Cabannes line vanishes due to coherent effects, but the other two 'incoherent' components remain. This cancellation is not apparent from the cross section, but arises from the summation over the scattering dipoles. The observation of the Rayleigh scattering requires dephasing of the scattered light. In the case of Placzek scattering, this dephasing comes from the random density fluctuations in the medium. In the forward direction there are no random phase shifts because the apparent Doppler shift seen in the scattered light is zero for any velocity. The other two components are still present because there is a random phase shift associated with the change of internal states of the dipole.

6. Lineshape

The Cabannes portion of the Rayleigh scattering is normally described as 'elastic' scattering. This corresponds to scattering that does not change the internal energy of the molecule. It excludes the Stokes and anti-Stokes rotational Raman scattering, as well as vibrational Raman scattering, but includes Placzek trace scattering and Q-branch rotational Raman scattering. Frequency shifts in the light do arise in these components from translational motion of the molecules, and it is those frequency shifts that are of particular interest for the measurement of flow parameters such as velocity, temperature, and density.

The line profile of this scattered light is a reflection of the motion of the molecules in the gas. The frequency of the scattered light will be shifted by the Doppler effect associated with that motion. One way to visualize this is shown in figure 6.

Here, $\vec{k}_1$ corresponds to the wave vector of the incident laser, and $\vec{k}_0$ is the wave vector of the light scattered to the observer. The incident laser is monochromatic, but the light scattered to the observer can have a number of different frequencies, all very close to the incident laser frequency. Each of these scattered frequencies can be considered separately as a monochromatic wave propagating to the observer. Since the

Table 5. (Forkey 1996). Differential scattering cross sections for each of the three components of scattered light, for incident light along the x-axis, and observation direction in the x–y-plane (given by $\theta = \theta_X$). Linearly polarized incident light is characterized by the angle β that it makes with respect to the z-axis. For natural, unpolarized incident light, β may be taken as $\pi/4$ (i.e., $\cos^2 \beta = \sin^2 \beta = 1/2$). The V or H superscripts refer to the vertical and horizontal polarization components of the incident light, and the V, H or 0 subscripts refer to the vertical, horizontal or total components of the scattered light.

$$\frac{\partial^\beta \sigma_i^j}{\partial \Omega} = \cos^2 \beta \frac{\partial^V \sigma_i}{\partial \Omega} \frac{^V K_i^j}{^V T_i} + \sin^2 \beta \frac{\partial^H \sigma_i}{\partial \Omega} \frac{^H K_i^j}{^H T_i} \qquad (5.1)$$

$$\frac{\partial^V \sigma_V}{\partial \Omega} = \frac{3\sigma}{8\pi} \frac{2 - \rho_0}{2 + \rho_0} \qquad \frac{\partial^H \sigma_V}{\partial \Omega} = \frac{3\sigma}{8\pi} \frac{\rho_0}{2 + \rho_0}$$

$$\frac{\partial^V \sigma_H}{\partial \Omega} = \frac{3\sigma}{8\pi} \frac{\rho_0}{2 + \rho_0} \qquad \frac{\partial^H \sigma_H}{\partial \Omega} = \frac{3\sigma}{8\pi} \frac{\rho_0 + (2 - 2\rho_0) \cos^2(\theta)}{2 + \rho_0} \qquad (5.2)$$

$$\frac{\partial^V \sigma_0}{\partial \Omega} = \frac{3\sigma}{8\pi} \frac{2}{2 + \rho_0} \qquad \frac{\partial^H \sigma_0}{\partial \Omega} = \frac{3\sigma}{8\pi} \frac{2\rho_0 + (2 - 2\rho_0) \cos^2(\theta)}{2 + \rho_0}$$
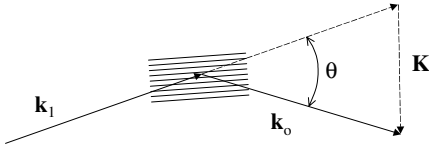

Figure 6. Scattering vector diagram. The incident wave vector is $\vec{k}_1$ and the scattered wave vector propagating to the observer is $\vec{k}_0$. These two vectors define an interference vector in the direction $\vec{K} = \vec{k}_0 - \vec{k}_1$ and an associated interference structure scale $\lambda_s = 2\pi/\vec{K}$.

incident laser beam and the observed light beam intersect in the sample volume, each observed frequency component creates an interference pattern, as shown in the diagram. Non-moving molecules have a scattering frequency component at the same frequency as the incident laser and these two single frequency waves generate a stationary interference pattern, as shown on the diagram. If the scattering is observed at an angle, θ, this interference pattern has a spatial frequency of

$$\lambda_s = \frac{\lambda_L}{2} \frac{1}{\sin \theta/2} \qquad (55)$$

in the direction $\vec{K} = \vec{k}_0 - \vec{k}_1$. The wave vector of the interference fringe is $|\vec{K}| = 2\pi/\lambda_s$. Any stationary molecules in this sample volume, or any molecules moving orthogonal to the $\vec{K}$ vector along the interference fringes, will scatter monochromatic light to the detector at the same frequency as the incident laser. If a monochromatic component at a different frequency than the incident laser is observed by the detector, a non-stationary interference or 'fringe' pattern is created. These fringes are swept along $\vec{K}$ at a rate proportional to the frequency difference between the incident laser and the shifted frequency component. Molecules that move along with this travelling interference pattern will continuously scatter at the shifted frequency. In the frame of the molecule both the incident and scattered light have the same frequencies. In this manner, each scattered frequency component can be pictured as arising from an interference pattern which moves at a velocity synchronized with the particle motion in the scattering medium. By analysing the frequency spectrum of the scattered light relative to the illumination laser frequency, one can extract a signal which is proportional to the number of molecules moving in each velocity interval. The velocity component observed is in the direction of the motion of the fringe pattern, in other words, in the direction $\vec{K} = \vec{k}_0 - \vec{k}_1$.

The utility of this moving interference pattern picture is that it gives some physical intuition as to the origin of the various components of the elastic scattering profile. If, for example, there is a non-zero average velocity, then the frequency shift, $\Delta\nu$, observed is written

$$\Delta\nu = \frac{1}{2\pi} \vec{v} \cdot \vec{K}. \qquad (56)$$

This can equivalently be written as

$$\Delta\nu = \frac{2v}{\lambda} \cos(\delta) \sin\left(\frac{\theta}{2}\right) \qquad (57)$$

where θ is the angle between k_0 and k_1 (the scattering angle), and δ is the angle between the velocity vector and $\vec{K}$. It should be clear that this scattering principle applies not only to molecules but also to small particles, clusters of molecules, density waves, or other scattering phenomena that may be present.

The spatial wavelength of the interference pattern imposes a spatial scale on the scattering volume. If spatial structures of density variations in the sample volume are on the same scale, then they strongly contribute to the detected signal (Grésillon and Mohamed-Benkadda 1988, Honoré 1996). If the mean free path of the molecule is small compared to the wavelength of the interference pattern, then density fluctuations caused by acoustic waves will be observable. If, on the other hand, the mean free path is longer than the wavelength of the interference pattern, then density waves will be spread out too far to contribute significantly to the scattering (Sandoval and Armstrong 1976).

In the low density or high temperature regime, the uncorrelated thermal motion of the molecules gives a symmetric Gaussian distribution centred about the mean velocity of the flow. In this case, the mean free path of the molecules is large compared to the grating wavelength, and, so, the scattering just reflects the motion of the molecules themselves. This is often called the thermally broadened Rayleigh line and corresponds to the Knudsen regime in gas kinetics. For a gas, at an absolute temperature T, the expression for the line profile is given by

$$g(\theta, T, \nu) = \frac{2}{\Delta\nu_T} \sqrt{\frac{\ln 2}{\pi}} \exp\left[-4 \ln 2 \left(\frac{\nu}{\Delta\nu_T}\right)^2 \right] \qquad (58)$$

where

$$\Delta\nu_T = \frac{|K|}{2\pi} \sqrt{\frac{8kT \ln 2}{m}} \qquad |K| = \frac{4\pi}{\lambda} \sin\left(\frac{\theta}{2}\right) \qquad (59)$$

and m is the mass of the molecule. Note that $g(\theta, T, \nu)$ integrated over ν is normalized to 1 and $\Delta\nu_T$ is defined as the full width at half maximum.

As the pressure of the gas increases, or the temperature decreases, the mean free paths of the molecules become shorter. When this mean free path becomes on the same order as the grating wavelength, then density fluctuations begin to contribute. The primary origin of these density fluctuations is acoustic waves travelling in the gas. Since the acoustic waves cause the density fluctuations to move at the acoustic propagation speed (the speed of sound), the scattering profile changes and acoustic sidebands appear (Landau and Placzek 1934). These acoustic sidebands are termed 'Brillouin–Mandel'shtam scattering', and, in high pressure media, they are sharply peaked. The region where the interference length, λ_s, is much greater than the mean free path corresponds to the hydrodynamic limit. In this regime there are three peaks which each have a Lorentzian shape. The two acoustic side bands are located at the frequency shift associated with the speed of sound in the medium, and the central peak is associated with the thermal diffusion rate, or, equivalently, the decay rate of the density fluctuation. The ratio of the total central peak intensity to the total sideband intensity for a single component gas is just $\gamma - 1$, where γ is the ratio of heat capacities (Clark 1975). This ratio becomes very large near the critical point, and it can depend strongly on the components of a gas mixture (Bot *et al* 1991). Other phenomena such as turbulent density fluctuations will also contribute to the scattering; however, in the optical regime, the typical interference wavelength is so short that these fluctuations can be neglected. In the infrared, however, particularly at small angles, the wavelengths can be much larger than the Kolmogorov scale, and turbulent density fluctuations can be primary contributors to the signal (Honoré 1996). For light gases such as helium, H_2, HD and D_2, Dicke narrowing must be taken into account (Gupta and May 1972).

In order to quantify the relative importance of the random versus the correlated acoustic motion of the molecules, a number of researchers have developed models to deal with this intermediate regime. The S6 model developed by Tenti *et al* (1974) is generally considered to be the most accurate for diatomic gases, but as pointed out by Young and Kattawar (1983), even that model is not exact. It assumes a single species and does not take into account the Q-branch of the rotational Raman scattering, which, as previously mentioned, falls in the elastic (Cabannes) scattering regime. The treatment of multi species is discussed by Letamendia *et al* (1981, 1982) and Baharudin *et al* (1972). These models all use a quantity called the y-parameter, which is essentially the inverse of a Knudsen number and is defined as the ratio of the scattering grating wavelength to the mean free path:

$$y \equiv \frac{\lambda_s}{2\pi\ell_m} \cong \frac{NkT}{\sqrt{2}|K|v_0\eta} \tag{60}$$

where N is the number density of the gas, η is the shear viscosity, $|K|$ is the magnitude of the scattering wave vector and v_0 is a velocity related to the thermal velocity.
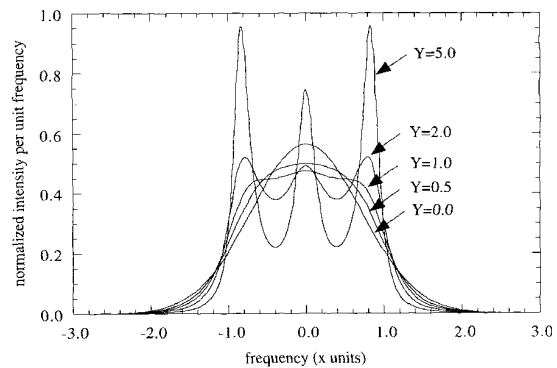
$$v_0 = \sqrt{\frac{kT}{m}}. \tag{61}$$

Figure 7. Rayleigh–Brillouin profiles for y-parameters ranging from 0 to 5. x is a normalized frequency parameter. The curves range from the kinetic regime (Boltzmann curve) to the hydrodynamic regime (triple peaked curve) (Forkey *et al* 1998).

If the ideal gas law is assumed, and the Sutherland formula for viscosity is used:

$$\eta = \eta_0 \left(\frac{T}{T_0}\right)^{3/2} \left(\frac{T_0 + S}{T + S}\right) \tag{62}$$

where η_0 is 1.716×10^{-5} N s m^{-2}, T_0 is 273 K, and S is 111 K for air, then the y-parameter becomes

$$y = 0.230 \left[\frac{T\,(\text{K}) + 111}{T^2\,(\text{K})}\right]\left[\frac{P\,(\text{atm})\lambda\,(\text{nm})}{\sin\theta/2}\right] \tag{63}$$

where P is the pressure in atmospheres, and λ is the laser wavelength in nm.

Figure 7 shows the Rayleigh–Brillouin scattering profiles calculated using the Tenti model for various y-parameters. In this figure the frequency is normalized in units of x:

$$x = \frac{2\pi\nu}{\sqrt{2}Kv_0} \tag{64}$$

where ν is the frequency shift from the line centre. If $y \gg 1$, then scattering is in the hydrodynamic regime where acoustic effects dominate, and if $y \ll 1$, scattering is in the thermal regime where acoustic effects can be neglected.

For standard air (1 atm, 298 K) observed at 532 nm light (frequency-doubled Nd:YAG laser), the y-parameter is 0.79, so acoustic effects must be taken into account. Figure 8 shows the form of the Cabannes line predicted by that model under those conditions.

7. Spectral filtering of Rayleigh light

Much recent work has focused on the development of spectral filters with two major goals in mind. The first goal has been to analyse the spectral properties of Rayleigh light so that temperature and velocity information can be extracted. The second goal is the suppression of background light which would otherwise obscure or contaminate the Rayleigh signal. The first goal, the measurement of temperature and velocity, requires the measurement of the spectral linewidth and the frequency shift of the light scatter. In the case of scattering from molecules, the frequency shift is small compared to the thermal linewidth except for supersonic flows. For example,
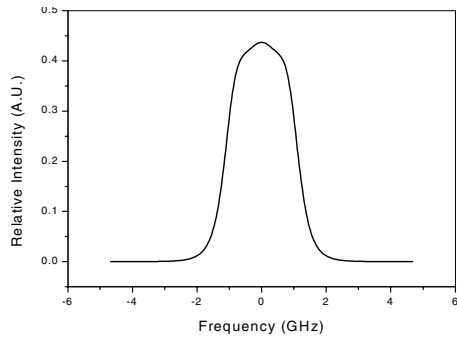
Figure 8. Tenti model for the Cabannes scattering lineshape for standard air observed at 90° with 532 nm light.
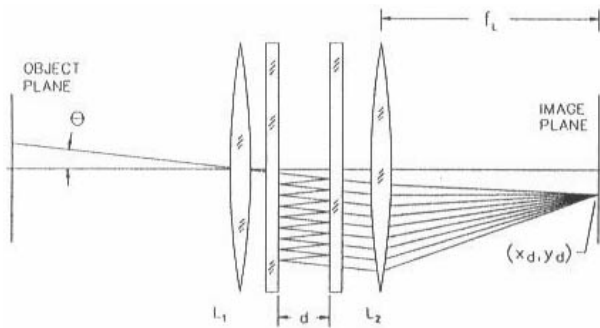

Figure 9. Fabry–Perot etalon configuration used for spectrally resolving planar images (Seasholtz *et al* 1997).

for collection at 90° using a frequency-doubled Nd:YAG laser at 0.532 micrometres wavelength, the frequency shift is 2.66 MHz (per metre per second). At atmospheric temperature, the thermal line broadening for air with the same geometry and laser is 1.83 GHz. This means that the measurement of flow velocity using Rayleigh scattering from molecules requires the determination of the line centre to approximately one part in 70 in order to determine flow velocity to an accuracy on the order of 10 metres per second. In the case of nanoscale particles, the mass is significantly larger, so the thermal linewidth is much smaller and the measurement of the velocity by spectral lineshift is more easily accomplished.

Optical filters that are capable of GHz or better resolution are either based on interference phenomena, such as the Fabry–Perot etalon, or on resonance features associated with atoms or molecules. The Fabry–Perot etalon has traditionally been the tool for resolving the Rayleigh spectrum, and recent work using an etalon in an imaging configuration has led to field measurements of temperature and velocity. As shown in figure 9 (Seasholtz *et al* 1997), the Fabry–Perot etalon consists of two reflective planar mirrors which are placed facing each other. Light passes through this etalon if the spacing between the mirrors is an integral number of half wavelengths. Otherwise, the light is reflected. By coating the mirrors with high reflectivity coatings, the transmission bandwidth of the etalon can be made exceptionally narrow so that it samples a small frequency interval within the spectrum of the Rayleigh light. As the separation between mirrors is changed, different frequency intervals are sampled and the Rayleigh spectrum is recreated.
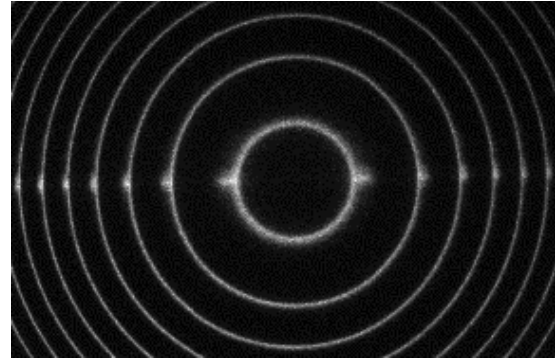

Figure 10. Fabry–Perot planar image of a supersonic jet. The distortion of the rings (along the horizontal axis) gives the velocity and temperature of the jet (Seasholtz *et al* 1997).

In a typical configuration, the light must pass through the etalon with its propagation vector perpendicular to the mirrors, which implies that the light comes from a point source on axis and is collimated into the etalon. This restricts the field of view to a small observation point. Generally, the separation of the mirrors is scanned using a piezoelectric driver so the transmission is swept across the spectrum of the light scattered from the point. This approach has been used, for example, to measure the broadening and frequency shift of the Rayleigh scattering in order to find the temperature and velocity of an argon thermal-plasma jet (Snyder *et al* 1993).

If the spacing between the plates is held constant, and the location of the point is moved off axis, as shown in figure 9, then the light passing through the etalon is no longer normal to the mirror faces, and transmission will only occur when the normal component of the propagation vector has the proper wavelength. For constant wavelength light, this means that the transmission will occur whenever

$$\frac{\lambda}{\cos\theta} = \frac{d}{2m} \qquad (65)$$

where d is the distance between the mirrors, θ is the angle of the light ray with reference to the normal to the mirrors and m is an integer. A lens following the etalon will generate an image of the light source. A planar source emitting a single frequency of light therefore generates an image of the source modulated in intensity by thin concentric light rings. Between concentric rings, the image is dark because the light cannot pass through the etalon. For spectrally broadened light, the rings broaden accordingly. Thus, if Rayleigh scattering from a flow field is imaged through an imaging Fabry–Perot set-up, the thickness of the rings can be used as a measurement of temperature. In addition, if there is an average velocity, the local position of the ring on the image is shifted. This approach has been used by Seasholtz and his colleagues to determine velocity and temperature contours in a supersonic jet. Figure 10 shows the Fabry–Perot image of a Mach 2 supersonic air jet where the displacement of the rings (along the centreline) gives a measure of the velocity (Seasholtz *et al* 1997). The Fabry–Perot filter has been used together with a LIDAR system to obtain Doppler spectral components for atmospheric temperature and wind measurements up to as high as 80 km (Tepley *et al* 1993).

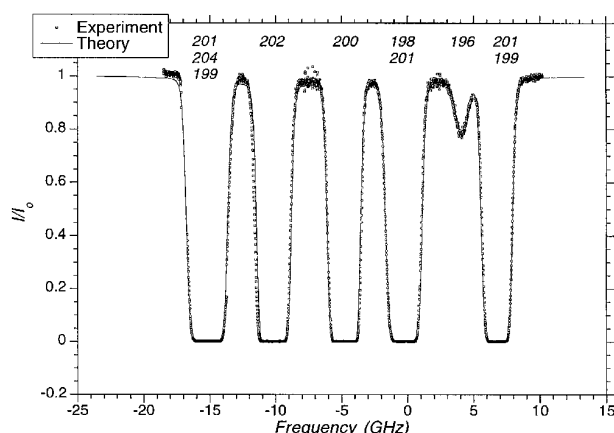Atomic and molecular filters provide an alternative approach to the measurement of the Rayleigh spectrum. In this

Figure 11. Transmission profile of mercury vapour notch absorption filter at 253.7 nm. The six observed absorption bands are due to the naturally occurring isotopes of mercury and to hyperfine splitting.
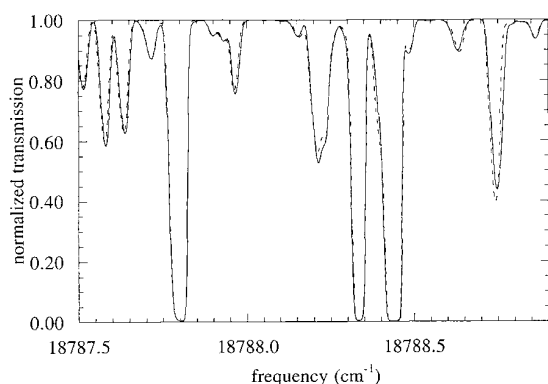

Figure 12. Transmission profile of an iodine vapour absorption filter in the vicinity of the frequency-doubled Nd:YAG laser line (Forkey *et al* 1997). The solid line represents the measured transmission and the dashed line represents the predicted transmission based on a corrected I_2 model.

case, a cell is filled with an atomic or molecular gas with a pressure, temperature and cell length chosen so very strong absorption occurs at an atomic or molecular resonance. If this absorption is optically thick, then there is an abrupt transition from absorption to transmission a few absorption linewidths away from the resonance peak. For example, the spectrum of an optically thick mercury vapour cell in the vicinity of the mercury resonance absorption at 254 nm is shown in figure 11 (Finkelstein 1997b). The various absorption lines are associated with various isotopic species, as indicated.

A similar type of structure is observed for iodine across the visible spectrum. For example, the iodine absorption in the vicinity of the frequency-doubled Nd:YAG laser line is shown in figure 12 (Forkey *et al* 1997). In both of these cases, the sharp transition from absorption to transmission can be used to analyse the Rayleigh scattering spectrum.

In the case of mercury, a narrow linewidth, frequency-tripled Ti:sapphire laser is tuned near the mercury absorption at 254 nm, and in the case of iodine, an injection-narrowed, frequency-doubled Nd:YAG laser is tuned in the vicinity of one of the iodine absorption features near 532 nm. The light scattered from the sample volume is passed through the vapour cell before being imaged onto a detector. As the laser is

scanned in frequency, the transmission of the scattered light passing through the cell varies, depending upon its Doppler-shifted, central frequency and spectral bandwidth in relation to the iodine absorption features (Forkey *et al* 1998). The transmission profile of light scattered off non-moving surfaces will just recreate the transmission profile of the cell itself. A moving surface gives the same transmission profile, but shifted in frequency. Rayleigh scattering from molecules is thermally, and, in some cases, acoustically broadened, and the transmission through the cell is a convolution of the absorption spectrum and the Rayleigh lineshape. Since the absorption spectrum is well known, this signal can be deconvolved to give a measurement of temperature, and, through the overall lineshift, a measurement of velocity. In figure 13 is a set of histograms showing the relative accuracy of this deconvolution process for the measurement of temperature, pressure, and velocity of stationary air taken with a narrow linewidth, tunable Nd:YAG laser and an iodine filter. Figure 14 shows the pressure, temperature and velocity structure in a slightly underexpanded Mach 2 free jet containing weak crossing shock structure (Forkey *et al* 1998).

The very strong resonant absorption which occurs in the cut-off region of the filter can be used to suppress background scattering that in many cases would otherwise obscure the Rayleigh signal. This feature has been used to suppress background scattering from particles in the atmosphere (Shimizu *et al* 1983, 1986) and is an important feature for the measurement of Rayleigh scattering near surfaces and ducts (Forkey 1994). Even if the air is not moving, the thermal motion of the molecules produces enough broadening to allow them to be seen when the laser is tuned to the absorption band of the filter. This approach can be used to increase the sensitivity of Rayleigh scattering in weakly ionized plasmas, where the high temperature produces significant broadening and the filter can be used to suppress background scattering from the plasma tube (Yalin and Miles 2000). It can also be used to suppress scattering from particulates such as soot which otherwise obscures Rayleigh measurements of combustion processes (Elliott *et al* 1997, Elliot and Beutner 1999, Hofmann and Leipertz 1996) and aerosol particles for temperature profile measurements in the atmosphere (Voss *et al* 1994, Shimizu *et al* 1986).

8. Rayleigh scattering from particles

The induced polarizability of a spherical particle whose circumference is much, much less than the wavelength of light is given by the expression (Jones 1979)

$$\alpha = 3\varepsilon_0 V \left(\frac{n^2 - 1}{n^2 + 2} \right) \tag{66}$$

where V is the volume of the particle and n is its index of refraction.

If the particle is truly spherical, there will be no depolarization, and this polarizability can be introduced into equation (5*b*) to obtain the intensity of the scattered light per particle. In terms of a differential cross section, the particle scattering is written

$$\frac{\partial \sigma}{\partial \Omega} = \frac{9\pi^2 V^2}{\lambda^4} \left(\frac{n^2 - 1}{n^2 + 2} \right)^2 \sin^2 \phi. \tag{67}$$
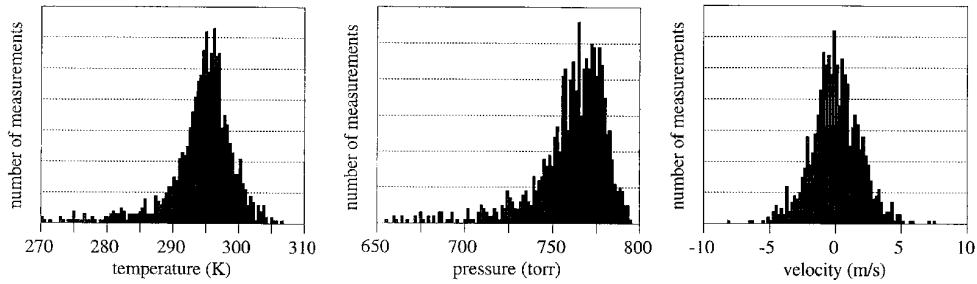
Figure 13. Histograms of the deconvolution of spectral data showing the measurement of temperature, pressure and velocity in stationary, room temperature air. Expected values are $\overline{T} = 295$ K, $\overline{P} = 759$ Torr and $\overline{v} = 0$ m s^{-1} (Forkey *et al* 1998).
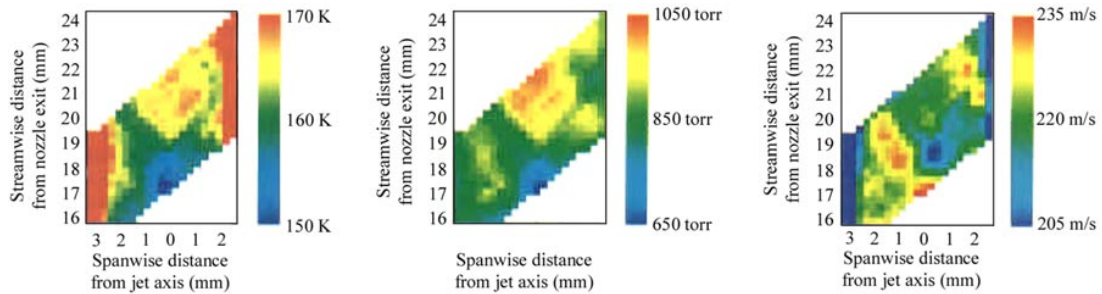

Figure 14. Temperature (left) pressure (centre) and velocity (right) measurements in a nearly pressure matched Mach 2 supersonic flow measured using Rayleigh scattering and fitting the Tenti profiles at each point in the image. Flow is from bottom to top and there is a weak crossing shock structure which shows up symmetrically in the measurements of scalar properties (pressure and temperature) but not in the velocity since the velocity component observed is off axis (Forkey *et al* 1998).
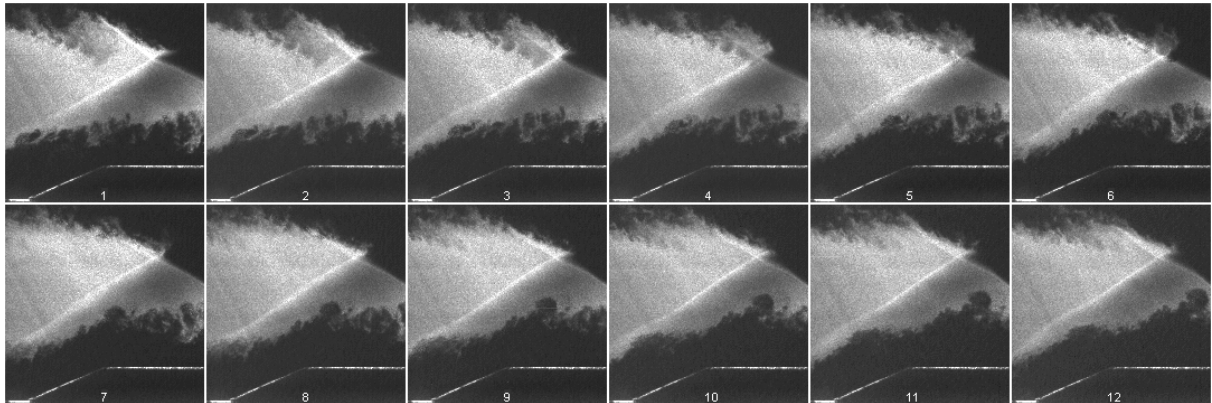

Figure 15. Rayleigh images of shock wave boundary layer interactions taken in a Mach 2.5 flow at 500 000 frames per second. Flow is from left to right and the scattering is from 10 nm scale CO_2 clusters, which condense in the cold portion of the flow, but not in the warmer portions corresponding to the boundary layers and behind strong shocks (Wu 1999, Wu *et al* 2000).

The total light scattering collected from the particles then becomes this differential cross section multiplied by the number of particles in the observation volume and integrated over the collection solid angle.

The dependence of this scattered signal on the square of the volume, which corresponds to the sixth power of the particle radius, heavily biases any observed signal towards larger diameter particles. The dominance of particle scattering can easily obscure scattering from the molecules and corrupt measurements of flow field properties. This is particularly true when some component of the gas condenses. For example, if 100 nm radius water droplets are present ($n = 1.33$), then even one of these droplets inside a 300 micron×300 micron×300 micron volume element will dominate the scattering from air at atmospheric pressure.

The large scattering cross section associated with small particles makes them attractive for flow field measurement and imaging, particularly when the flow density or the Rayleigh scattering cross section of the molecules in the flow is so low that the measurement or image would otherwise be unacceptably noisy or below the detection limit. Dielectric (nonabsorbing) particles with diameters less than approximately 100 nm fall into the 'Rayleigh' range and can be treated using the Rayleigh scattering formalism. Larger particles have more complex scattering patterns associated with optical interference and are treated using Thomson scattering theory (Fournier and Evans 1993). Nanoscale particles follow even highly fluctuating fluid flows very accurately, and fogs of such particles tend to be uniformly disbursed with many particles per resolution element. As a
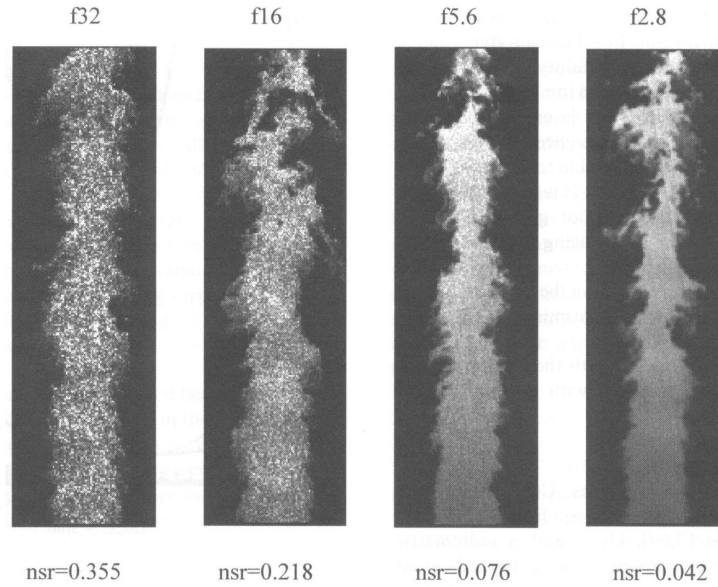
f32   f16   f5.6   f2.8

nsr=0.355   nsr=0.218   nsr=0.076   nsr=0.042

Figure 16. Image of Rayleigh scattering from water and CO_2 particles condensed in a Mach 1.36 air jet showing speckle effects for different camera f-stop settings. The noise to signal ratio is given at the bottom of each image (Elliot and Beutner 1999).
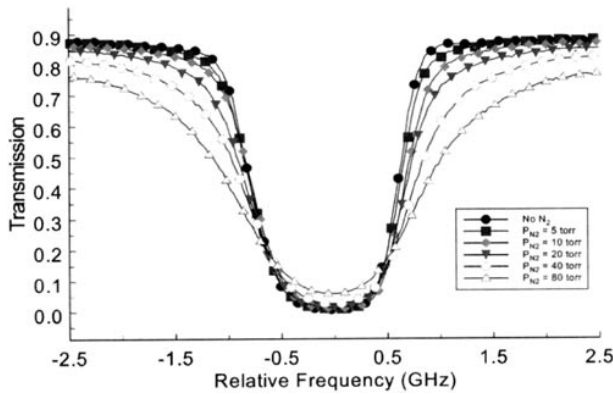

Figure 17. Iodine filter transmission profile as a function of nitrogen-buffered gas pressure (Mosedale *et al* 1998).

consequence, Rayleigh scattering from particulate fogs has become a useful method for the measurement of flow field velocity and imaging of flow structure. For example, 12 sequential images of shock wave–boundary layer interactions are shown using Rayleigh scattering from CO_2 ice fog in a Mach 2.5 air flow at 500 000 frames per second in figure 15. (Wu 1999, Wu *et al* 2000). The boundary layer and the region behind the shock–shock interaction are dark because they are at a higher temperature than the core flow, so the CO_2 is not condensed. In these images the flow is from left to right and the shock is generated by a wedge seen at the bottom of the images. These particles are estimated to be of the order of 10 nm in diameter, so they fall well within the Rayleigh range (Erbland *et al* 2000).

Scattering from nanoscale particulates differs from molecular Rayleigh scattering in that the thermal motion of the particles is substantially reduced due to their large mass in relation to the molecules. This has two consequences. The first is that the temperature cannot be measured as it can be with molecules since the mass of the individual particles is not

known with sufficient accuracy. The velocity, however, can be measured since the particles do travel with the flow. The second consequence is that the light that is scattered from the particles is significantly more coherent than that scattered from molecules, leading to interference phenomena, or 'speckle', at the image plane. In the case of randomly moving scatterers, the coherence time can be approximated as one over the thermal linewidth of the scattered light. In the case of molecules at room temperature, the thermal linewidth is on the order of a GHz or so for scattering in the visible, and the coherence time is less than a nanosecond. This means that any interference patterns in the image plane will only persist for on the order of a nanosecond, and over the time period of 10 ns or so, which is the characteristic time associated with most pulsed, high-power lasers, the interference pattern averages out. For particles, on the other hand, the thermal broadening may be on the order of tens of megahertz, leading to coherence times in excess of 100 nanoseconds. In this case, the interference pattern does not average out during the laser pulse time and 'speckle' is observed. The spatial frequency of the speckle pattern is determined by the phase difference between light rays. If the light is collected through a small aperture, the maximum phase difference is small and the speckle pattern features are large. If, on the other hand, the collection aperture is large, that phase difference is large and the speckle pattern becomes much finer. The scale of the speckle pattern is, therefore, proportional to the ratio of the distance between the lens and the image plane, d, and the lens diameter, D:

$$\lambda_{sp} \cong \lambda \frac{d}{D}. \tag{68}$$

This can be written in terms of the f-number of the lens (lens focal length to diameter ratio) and the magnification, M:

$$\lambda_{sp} = \lambda f^{\#}(1 + M). \tag{69}$$

If the spatial frequency of the speckle pattern is significantly smaller than the resolution scale of the detector, then the
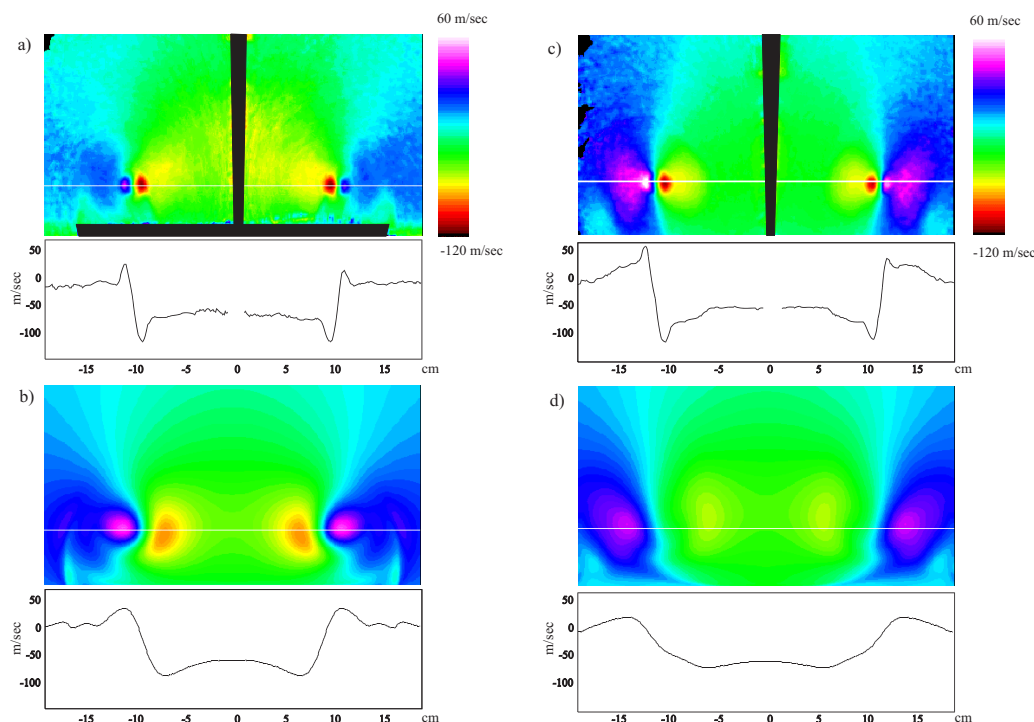
Figure 18. Images of the measured velocity field (upper images) over a delta wing at 97% of root chord (a) and 114% of the root chord (b) compared to computed results (c and d) (Elliot and Beutner 1999, Rizzetta 1996).

fringes are averaged and the speckle pattern is no longer observed. This means that large diameter-to-focal-length ratio lenses minimize speckle effects. Speckle is also minimized by using low magnification and short wavelength light scattering. Figure 16 shows the effect of the collection f-stop of the camera on the speckle (Elliot and Beutner 1999). In these images, the condensation of naturally occurring water vapour and CO_2 in a Mach 1.36 air jet appears rather uniform at low f-stops (large collection aperture), but extremely speckled at high f-stops (small collection aperture). At the bottom of each image is the measure of the noise to signal ratio.

9. Planar Doppler velocimetry

A major limitation of molecular Rayleigh scattering is the small scattering cross section, and, consequently, the requirement for either very high power lasers or long integration times. In addition, the thermal broadening associated with the molecules makes the measurement of velocity relatively difficult. Both of these problems can be mitigated by using nanoscale particles rather than molecules as scattering centres. The relatively large mass associated with the nanoscale particles in comparison with molecules reduces the thermal broadening and makes the velocity measurement more robust. In addition, the very strong scattering from these particles reduces the illumination energy requirements and gives better signal to noise. If these nanoscale particles are mono-dispersed into a particle fog, then they can be used to image flow density variations as well as the velocity. Of particular interest is the use of a molecular filter to determine the velocity of the particles, and by inference, the flow field itself. The concept of using molecular filters to measure the velocity of particles was

first called doppler Global velocimetry (Meyers and Komine 1991), but work in this area has now come to be known as planar Doppler velocimetry (Clancy and Samimy 1997, Samimy and Wernet 2000). This approach is particularly useful for imaging mixing and structure in high speed flow fields (Clancy *et al* 1999, Smith and Northam 1996, McKenzie 1996).

For these experiments, the particle fog is usually created by some condensing material such as water vapour, carbon dioxide or ethanol. In a supersonic flow, the temperature drops rapidly through the expansion nozzle and these seed gases at concentrations on the order of 1% or less (Erbland 2000) condense into nanoscale particulate fogs, which are observed as they pass through the test section. The velocity measurements can then be made in two ways. The first is by scanning the laser frequency and recording the transmission through an iodine cell in much the same way measurements are made for molecular Rayleigh scattering. The second approach is to keep the laser frequency constant at a frequency selected such that the velocity-shifted light falls at the 50% transmission point of the cell cut-off curve. Variations in the frequency around this point due to the Doppler shifts of scattered light then correspond to variations in the transmission of the cell, and there is a 1:1 correspondence between the transmissivity and the velocity. Thus, by measuring the intensity distribution and referencing that to an unfiltered image of the same flow field, the velocity field is measured. Since the cut-off slope of a pure atomic or molecular vapour filter is sharp, only a narrow range of velocities can be recorded in this manner before the filter reaches either full transmission or strong absorption. The filter profile can be broadened with the addition of a buffer gas such as nitrogen in order to extend this range, if necessary. Figure 17 shows the iodine filter transmission profile as a function of nitrogen-buffered gas pressure (Mosedale *et al* 1998). This

type of cell has been used in various experiments to capture velocity fields in supersonic jets and vorticity fields in subsonic flows. For example, figure 18 shows the velocity field near the trailing edge of a 70° swept delta wing at a 23° angle of attack (Elliot and Beutner 1999, Mosedale 1998). The PDV approach has been used to acquire single and multicomponent velocity fields in complex flows (see, for example, Arnette *et al* 1998, Smith and Northam 1996, Meyers 1995).

10. Summary

Laser Rayleigh scattering from both molecules and nanoscale particles is an increasingly useful tool for diagnostics of gases. Measurements made with high power, short pulse length lasers can now freeze a density field in time, and generate quantitative measures of complex structures. This is particularly useful in high speed flows where shock waves and boundary layer structure have large associated density fluctuations which can be easily visualized using Rayleigh imaging. Point measurements with continuous lasers can be used to study time variations of flows and can be swept to produce time averaged images. The fact that Rayleigh scattering occurs at any wavelength means that the laser wavelength can be chosen to optimize other factors. For example, if an atomic or molecular filter is to be used for detection, the laser wavelength can be chosen close to the resonance of that filter. Since frequency shifts associated with Rayleigh scattering are constant over small changes in wavelength, the laser can be tuned, thereby tuning, in turn, the Rayleigh scattering. In this manner, the Rayleigh scattered light can be tuned across the spectrally relevant wavelength region of the filter. Thus, the filter can be optimized for light collection, spectral sensitivity and imaging. The recent development of the injection-locked laser, together with high discrimination optical filters, has now led to the feasibility of using Rayleigh scattering for velocity and temperature measurements. The fact that the signal is scattered 'instantaneously' from the molecules means that the signal strength is largely unaffected by molecular collisions, in contrast to other diagnostics such as laser-induced fluorescence, where quenching and collisional line broadening must be taken into account. Nanoscale particles improve the signal level and may be particularly useful for field measurements of velocity structures. These new technologies are continuing to evolve with new high power, injection-locked ultraviolet lasers on the horizon. These lasers will significantly improve Rayleigh scattering signals through the frequency to the fourth power dependence of the Rayleigh cross section. With these technologies and new filters based on ultraviolet transitions such as in mercury vapour, it is expected that Rayleigh scattering will become an increasingly useful tool for fluid dynamics and combustion laboratories.

References

Abhyankar K D 1996 Hundred and twenty-five years of Rayleigh scattering in the study of the planetary atmospheres *Q. J. R. Astron. Soc.* **37** 281

Arnette S A, Samimy M and Elliott G S 1998 Two-component planar Doppler velocimetry in the compressible turbulent boundary layer *Exp. Fluids* **24** 323

Baharudin B Y, Schoen P E and Jackson D A 1972 Light scattering in the gas mixture helium–krypton *Phys. Lett.* A **42** 77

Bates D R 1984 Rayleigh scattering by air *Planet. Space Sci.* **32** 785

Born M and Wolf E 1980 *Principles of Optics* 6th edn (Oxford: Pergamon) p 98

Bot A, Schaink H M, Schram R P C and Wegdam G H 1991 Rayleigh–Brillouin light scattering from noble gas mixtures. 1. The Landau–Placzek Ratio *J. Phys. Chem.* **95** 4673

Bucholtz A 1995 Rayleigh scattering calculations for the terrestrial atmosphere *Appl. Opt.* **34** 2765

Clancy P S and Samimy M 1997 Two component planar Doppler velocimetry in high-speed flows *AIAA J.* **35** 1729

Clancy P S, Samimy M and Erskine W R 1999 Planar Doppler velocimetry: three-component velocimetry in supersonic jets *AIAA J.* **37** 700

Clark N A 1975 Inelastic light scattering from density fluctuations in dilute gases. The kinetic–hydrodynamic transition in a monatomic gas *Phys. Rev.* A **12** 232

Dam N J, Rodenburg M, Tolboom R A L, Stoffels G G M, Husiman-Kleinherenbrink P M and ter Meulen J J 1998 Imaging of an underexpanded nozzle flow by UV laser Rayleigh scattering *Exp. Fluids* **24** 93

Dibble R W and Hollenbach R E 1981 Laser Rayleigh thermometry in turbulent flames *18th Symp. (Int.) on Combustion* (Combustion Institute) p 1489

Dyer T M 1979 Rayleigh scattering measurements of time-resolved concentration in a turbulent propane jet *AIAA J.* **17** 912

Elliot G S and Beutner T J 1999 Molecular filter based planar Doppler velocimetry *Prog. Aerospace Sci.* **35** 799

Elliott G S, Glumac N, Carter C D and Nejad A S 1997 Two-dimensional temperature field measurements using a molecular filter based technique *Combust. Sci. Technol.* **125** 351

Erbland P J, Rizzetta D P and Miles R B 2000 Numerical and experimental investigation of CO_2 condensate behavior in hypersonic flow *21st AIAA Aerodynamic Measurement Technology and Ground Testing Conf. (Denver, CO, 2000)* paper AIAA-2000-2379

Escoda M C and Long M B 1983 Rayleigh scattering measurements of the gas concentration field in turbulent jets *AIAA J.* **21** 81

Finkelstein N D, Lempert W R and Miles R B 1997a Narrow-linewidth passband filter for ultraviolet rotational Raman imaging *Opt. Lett.* **22** 537

——1997b Narrow linewidth passband filters and UV laser source for rotational Raman imaging *SPIE* **3172** 656–65

Finkelstein N D, Yalin A P, Lempert W R and Miles R B 1998 Dispersion filter for spectral and spatial resolution of pure rotational Raman scattering *Opt. Lett.* **23** 1615

Forkey J N 1996 Development and demonstration of filtered Rayleigh scattering—a laser-based flow diagnostic for planar measurement of velocity, temperature and pressure *PhD Thesis* Princeton University MAE Department

Forkey J N, Lempert W R and Miles R B 1997 Corrected and calibrated I_2 absorption model at frequency-doubled Nd:YAG laser wavelengths *Appl. Opt.* **36** 6729

——1998 Accuracy limits for planar measurements of flow field velocity, temperature and pressure using filtered Rayleigh scattering *Exp. Fluids* **24** 151

Forkey J N, Lempert W R, Bogdonoff S M, Miles R B and Russell G 1994 Volumetric imaging of supersonic boundary layers using filtered Rayleigh scattering background suppression *AIAA 32nd Aerospace Sciences Meeting Exhibit. (Reno, NV)* paper AIAA 94-0491

Fournier G R and Evans B T N 1993 Bridging the gap between the Rayleigh and Thomson limits for spheres and spheroids *Appl. Opt.* **32** 6159

Grésillon D and Mohamed-Benkadda M S 1988 Direct mode–mode coupling observation in the fluctuations of non-stationary transparent fluid *Phys. Fluids* **31** 1904

Gupta B K and May A D 1972 Dicke narrowing and collision broadening of the depolarized Rayleigh and $S_0(1)$ Raman line

in the hydrogen isotopes and H_2–He, H_2–Ne mixtures *Can. J. Phys.* **50** 1747

Hofmann D and Leipertz A 1996 Temperature field measurements in a sooting flame by filtered Rayleigh scattering (FRS) *26th Symp. (Int.) on Combustion* (Combustion Institute) p 945

Honoré C 1996 Le signal complexe de la diffusion collective de la llumiere et les ecoulements turbulents *Doctoral Thesis* L'Ecole Polytechnique, Marseille

Jackson 1998 *Classical Electrodynamics* (New York: Wiley)

Jones A R 1979 Scattering of electromagnetic radiation in particulate laden fluids *Prog. Energy Combust. Sci.* **5** 73

Kattawar G W, Young A T and Humphreys T J 1981 Inelastic scattering in planetary atmospheres. I. The ring effect, without aerosols *Astrophys. J.* **243** 1049

Landau L and Placzek G 1934 Structure of the undisplaced scattering line *Phys. Z. Sowiet. Un.* **5** 172

Letamendia L, Chabrat J P, Nouchi G, Rouch J and Vaucamps C 1981 Light scattering studies of moderately dense gas mixtures: hydrodynamic regime *Phys. Rev.* A **24** 1574

Letamendia L, Joubert P, Chabrat J P, Rouch J, Vaucamps C, Boley C D, Yip S and Chen S H 1982 Light scattering studies of moderately dense gases. 2. Non-hydrodynamic regime *Phys. Rev.* A **25** 481

Long D A 1977 *Raman Spectroscopy* (New York: McGraw-Hill) section 3.4.3, p 57

Long M B, Philip S L and Fourguette D C 1985 Simultaneous two-dimensional mapping of species concentration and temperature in turbulent flames *Opt. Lett.* **10** 267

McKenzie R L 1996 Measurement capabilities of planar Doppler velocimetry using pulsed lasers *Appl. Opt.* **35** 948

Meulenbroeks R F G, Schram D C, Jaegers L J M and van de Sanden M C M 1992 Depolarization Rayleigh scattering as a means of molecular concentration determination in plasmas *Phys. Rev. Lett.* **69** 1379

Meyers J F 1995 Development of Doppler global velocimetry as a flow diagnostic tool *Meas. Sci. Technol.* **6** 769

Meyers J F and Komine H 1991 Doppler Global velocimetry: a new way to look at velocity *Laser Anemometry* **1** 296–8

Miles R B and Lempert W R 1997 Quantitative flow visualization in unseeded flows *Annu. Rev. Fluid. Mech.* **29** 285

Mosedale A D, Elliott G S, Carter C D, Weaver W L and Beutner T J 1998 On the use of planar Doppler velocimetry *29th AIAA Fluid Dynamics Conf. (Albuquerque, NM)* paper AIAA-98-2809

Naus H and Ubachs W 2000 Experimental verification of Rayleigh scattering cross sections *Opt. Lett.* **25** 347

Panda J and Seasholtz R G 1999 Measurement of shock structure and shock–vortex interaction in underexpanded jets using Rayleigh scattering *Phys. Fluids* **11** 3761

Penney C M 1969 Light scattering in terms of oscillator strengths and refractive indices *J. Opt. Soc. Am.* **59** 34

Pitz R W, Cattolica R, Robben F and Talbot L 1976 Temperature and density in a hydrogen air flame from Rayleigh scattering *Combustion Flame* **27** 313

Reckers W, Gu Y, Rothe E W and Voges H 1997 Rayleigh scattering of excimer laser light from some simple molecules at 193 nm and 248 nm: the effect of polarization upon imaging diagnostics *Appl. Spectrosc.* **51** 1012

Richards C D and Pitts W M 1993 Global density effects on the self-preservation behaviour of turbulent free jets *J. Fluid Mech.* **254** 417

Rizzetta D 1996 Numerical simulations of the interaction between a leading edge vortex and a vertical tail *AIAA Paper* 96-2012

Rowell R L and Aval G M 1971 Rayleigh–Raman depolarization of laser light scattered by gases *J. Chem. Phys.* **54** 1960

Sabbaghzadeh J, Buell W, Holder J and Fink M 1995 A very narrow, high throughput Rayleigh filter for Raman spectroscopy *Appl. Phys.* B **60** S261

Samimy M and Wernet M P 2000 Review of planar multiple component velocimetry in high-speed flows *AIAA J.* **38** 553

Sandoval R P and Armstrong R L 1976 Rayleigh–Brillouin spectra in molecular nitrogen *Phys. Rev.* A **13** 752

Seasholtz R G, Buggele A E and Reeder M F 1997 Flow measurements based on Rayleigh scattering and Fabry–Perot interferometer *Opt. Lasers Eng.* **27** 543

Shimizu H, Lee S A and She C Y 1983 High spectral resolution LIDAR system with atomic blocking filters for measuring atmospheric parameters *Appl. Opt.* **22** 1373

Shimizu H, Noguchi K and She C Y 1986 Atmospheric-temperature measurement by a high spectral resolution LIDAR *Appl. Opt.* **25** 1460

Sica R J *et al* 1995 Lidar measurements taken with a large-aperture liquid mirror. F1. Rayleigh scatter system *Appl. Opt.* **34** 6925

Smith M W and Northam G B 1996 Application of absorption filter-planar Doppler velocimetry to sonic and supersonic jets *AIAA J.* **34** 434

Snyder S C, Reynolds L D, Lassahn G D, Fincke J R, Shaw C B Jr and Kearney R J 1993 Determination of gas temperature and velocity profiles in an argon thermal-plasma jet by laser light scattering *Phys. Rev.* E **47** 1996

Stanton S G and Pecora R 1981 Resonance enhanced dynamic Rayleigh scattering *J. Chem. Phys.* **75** 5615

Tenti G, Boley C D and Desai R C 1974 On the kinetic model description of Rayleigh–Brillouin scattering from molecular gases *Can. J. Phys.* **52** 285

Tepley C A, Sargoytchev S I and Rojas R 1993 The Doppler Rayleigh lidar system at arecibo *IEEE Trans. Geosci. Remote Sensing* **31** 36

Van de Hulst H C 1957 *Light Scattering by Small Particles* (New York: Dover)

Voss E, Weitkamp C and Michaelis W 1994 Lead-vapour filters for high spectral resolution temperature LIDAR *Appl. Opt.* **33** 3250

Wu P 1999 MHz-rate, pulse-burst laser imaging system: development and application in the high-speed flow diagnostics *PhD Thesis* Princeton University MAE Department

Wu P, Lempert W R and Miles R B 2000 Megahertz pulse-burst laser and visualization of shock wave/boundary layer interaction *AIAA J.* **38** 672

Yalin A P and Miles R B 2000 Temperature measurements by ultraviolet filtered Rayleigh scattering using a mercury filter *J. Thermophys. Heat Transfer* **14** 210

Young A T 1981 Rayleigh scattering *Appl. Opt.* **20** 533

——1982 Rayleigh scattering *Phys. Today* **35** 42

Young A T and Kattawar G W 1983 Letters to the editor—Rayleigh scattering line profiles *Appl. Opt.* **22** 3668